



<b>Publication Year</b>	2020
<b>Acceptance in OA @INAF</b>	2022-01-18T15:26:27Z
<b>Title</b>	Preliminary estimation of the detection possibilities of Ganymede's water vapor environment with MAJIS
<b>Authors</b>	PLAINAKI, CHRISTINA; SINDONI, Giuseppe; GRASSI, Davide; Cafarelli, L; D'AVERSA, EMILIANO; et al.
<b>DOI</b>	10.1016/j.pss.2020.105004
<b>Handle</b>	<a href="http://hdl.handle.net/20.500.12386/31331">http://hdl.handle.net/20.500.12386/31331</a>
<b>Journal</b>	PLANETARY AND SPACE SCIENCE
<b>Number</b>	191

**Preliminary estimation of the detection possibilities of Ganymede's water vapor environment  
with MAJIS**

Christina Plainaki (1), Giuseppe Sindoni (1), Davide Grassi (2), Luigi Cafarelli (1)(3), Emiliano D'Aversa (2), Stefano Massetti (2), Alessandro Mura (2), Anna Milillo (2), Gianrico Filacchione (2), Giuseppe Piccioni (2), Yves Langevin (4), Francois Poulet (4), Federico Tosi (2), Alessandra Migliorini (2), Francesca Altieri (2)

(1) Italian Space Agency, Rome, Italy ([christina.plainaki@asi.it](mailto:christina.plainaki@asi.it))

(2) INAF - Institute of Space Astrophysics and Planetology, Rome, Italy

(3) University of Tor Vergata, Rome, Italy

(4) Institut d'Astrophysique Spatiale, Orsay, France.

**Abstract**

The exosphere of Ganymede is the interface region linking the moon's icy surface to Jupiter's magnetospheric environment. Its characterization is of key importance to achieve a full understanding of the ice alteration processes induced by the radiation environment. Several scientific instruments that will operate on board the upcoming Jupiter Icy Moons Explorer (JUICE) mission, selected by ESA in the context of its Cosmic Vision programme, have the potential to study Ganymede's exosphere. Among them, the Moons And Jupiter Imaging Spectrometer (MAJIS) will have the chance to investigate the composition of the moon's exospheric components and the emission of water molecules. The exospheric water density profile, as obtained from current models, is a crucial parameter for the estimation of the expected signal to noise ratio related to the actual measurement. In lack of an adequate number of Ganymede's observations from past missions, there is a general

difficulty in constraining current exosphere models which are based, in general, on different scenarios and considerations and often show large discrepancies in the estimated spatial distribution of the neutral environment. In this work, we make a preliminary estimation of the expected IR emission from exospheric water molecules, using different modelled density profiles, and we speculate on the possibility of JUICE/MAJIS to detect it. An exercise on the potential plume detection capabilities of MAJIS is also performed. The first necessary step for performing these calculations is a rough comparison of the existing models of Ganymede's water vapor exosphere. We discuss the characteristics of the neutral environment as derived from different exospheric models available in literature, the role of the ion-surface interactions in the H<sub>2</sub>O exosphere generation, and the related implications also in view of future observations. We then use the model outputs to estimate different scenarios for the expected non-Local Thermal Equilibrium (non-LTE) emission from these molecules. The results of this study can be of help during the JUICE observation planning phase.

## **1. Introduction: general concept and motivation for the current work**

Ganymede is the only known moon in the Solar System so far explored to possess an intrinsic magnetic field embedded within a planetary magnetosphere (Gurnett et al., 1996; Kivelson et al., 1996; 1998). The intensity of Ganymede magnetic field, up to ~1,500 nT in the polar regions (Williams et al., 1997), is sufficiently strong to stand off the Jovian plasma flow, as revealed by the measurements of the Energetic Particle Detector (EPD) onboard the Galileo mission (Williams et al., 1992), in the vicinity of the moon and within its magnetosphere (e.g., Paranicas et al., 1999; Williams, 2001). A non-negligible flux of charged particle populations (mainly Hydrogen, Oxygen and Sulfur ions) impacting the moon's icy surface is believed to activate different release processes, such as sputtering and radiolysis (Marconi, 2007; Plainaki et al., 2015; Leblanc et al., 2017). Modeling of the ion circulation around Ganymede has shown that the bulk population of Jupiter's plasma sheet enters

the moon's magnetosphere mainly through the cusps and at low latitudes in the plasma wake hemisphere, most likely through tail reconnection (Pope et al., 2018). The energetic ions in the keV-MeV range are expected to impact the moon also at regions outside the cusps (see, for instance, Plainaki et al., 2015), inducing ice dissociation and direct sputtering of surface molecules (Bahr et al., 2001; Moore et al., 2007; Teolis et al., 2006, 2017). Laboratory studies revealed that a series of complex surface chemistry processes initiated after ice bombardment by energetic ions, results in the release of H, H<sub>2</sub>, O, O<sub>2</sub>, OH, and H<sub>2</sub>O particles (Johnson, 1990). The characteristics of the energetic particles in the vicinity of the Galilean moons and the release of particles from their icy surfaces have been discussed in the fundamental paper by Cooper et al. (2001). At Ganymede, the ion-induced particle release, together with water sublimation, are believed to generate a tenuous atmospheric envelope around the moon, often referred to as an "exosphere" (e.g., Plainaki et al., 2015). The measurements by the Plasma Science (PLS; Frank et al., 1997b) and Plasma Wave Science (PWS; Eviatar et al., 2001) instruments onboard Galileo, revealed that Ganymede also possesses an ionosphere (Carnielli et al., 2019), consistently with the findings of the Galileo radio occultation experiment (Kliore, 1998).

Globally, the exosphere of Ganymede consists mainly of sputtered H<sub>2</sub>O as well as O<sub>2</sub> and H<sub>2</sub> produced through radiolysis (Johnson, 1990); some other minor species are also expected to be released from the surface through sputtering. The global exospheric environment, therefore, is expected to be formed through a complex process driven by the energy and spatial distributions of the Jovian ion populations, depending at the same time on the moon surface characteristics (e.g. temperature, composition) and the particle release properties (yield, initial energy distribution). Ganymede's neutral environment is believed to be mainly collisionless apart a limited region around the subsolar point where collisions may be present (Marconi, 2007). The exosphere of Ganymede is the actual interface between the icy surface of this moon and Jupiter's magnetosphere. Therefore, its characterization is of key importance to achieve a full understanding of the ice alteration processes

induced by the radiation environment, similarly to the case of Europa (see, for instance, Plainaki et al., 2018 and references therein). For example, the deposition of neutral species from the exosphere onto the moon's surface (e.g., deposition of water) will spectrally mask the weathering products or directly start new chemical patterns. Moreover, the efficiency of both surface weathering and particle release from the surface may be reduced by the ionosphere, which is formed by the ionization of the neutral exosphere. In this view, a number of numerical models have been developed to understand the plasma circulation around this moon as well as the generation of its surface-bounded H<sub>2</sub>O exosphere (e.g., Marconi 2007; Turc et al., 2014; Plainaki et al., 2015; Shematovich 2016; Leblanc et al., 2017) and ionosphere (Carnielli et al., 2019). Some evidence for the existence of an exosphere around Ganymede was already provided by the Galileo/UVS (Barth et al., 1996), the HST/GHRS (Hall et al., 1998) and HST/STIS (Feldman et al., 2000) instruments. Recently, the Heterodyne Instrument for the Far Infrared (HIFI) on board the Herschel Space Observatory (Hartogh et al., 2013) observed the vapor H<sub>2</sub>O environment of Ganymede. These authors found a difference between the H<sub>2</sub>O densities observed at the leading and trailing hemispheres of a factor of 10 and they attributed it to surface composition characteristics, although the uncertainty in their measurements is not negligible.

Several scientific instruments that will operate on board ESA's upcoming Jupiter Icy Moons Explorer (JUICE) mission, have the potential to study Ganymede's H<sub>2</sub>O exosphere (Grasset et al., 2013; JUICE definition study report<sup>1</sup>). Among them, the Moons And Jupiter Imaging Spectrometer (MAJIS) will investigate the composition and spatial distribution of water and non-water-ice components in both Ganymede's surface and exospheric environment. There is a strong scientific motivation for speculating on the potential of observing Ganymede's H<sub>2</sub>O exosphere during ESA's upcoming JUICE mission. In particular, revealing the characteristics of the near-surface H<sub>2</sub>O environment along

---

<sup>1</sup> <http://sci.esa.int/juice/54993-juice-definition-study-report-red-book/>

103 Ganymede's orbit around Jupiter will allow the identification of its source regions and also the  
104 efficiency of the particle release from ice, providing at the same time constraints for estimating the  
105 energy exchange between the Jovian system and the moon itself. This is due to the fact that the spatial  
106 density and energy distributions of Ganymede's H<sub>2</sub>O environment reflect the origins of the exosphere  
107 generation and the properties of the interaction of the icy surface with the moon's surrounding  
108 radiation environment. Indeed, the morphology of the sputtered-H<sub>2</sub>O exosphere depends on the  
109 topology of the open/closed magnetic field line region, the incident Jovian ion flux and the content  
110 of ice contaminants on the surface. In particular, the H<sub>2</sub>O molecules released from the surface after  
111 its bombardment by Jupiter's plasma and energetic ions follow ballistic trajectories until they return  
112 to the surface or they escape or they are lost through ionization or dissociation processes. Upon return  
113 to the surface, the H<sub>2</sub>O molecules stick there and do not migrate to nearby locations hence remaining  
114 confined to their ejection region. This is an important distinction between the H<sub>2</sub>O and the O<sub>2</sub>  
115 exospheric components. In fact, the O<sub>2</sub> molecules, upon return to the surface, they get thermalized  
116 (average kinetic energy  $\sim k_b T$ ) and bounce back to continue their ballistic travel. The process of  
117 thermal desorption after the re-impacting of the molecules to the surface is repeated many times until  
118 O<sub>2</sub> is either dissociated or ionized. Consequently, contrary to the sputtered-H<sub>2</sub>O case, the spatial  
119 distribution of the O<sub>2</sub> exospheric density is not directly coupled to its production map upon the  
120 surface. Since the H<sub>2</sub>O molecules lifetime (before loss) is much longer than the average ballistic flight  
121 time, and due to the water's sticking to the ice capability, the spatial distribution of the H<sub>2</sub>O exosphere  
122 maintains the memory of its origins, providing information on the spatial characteristics of the ice –  
123 ion interaction as well as on the sputtering efficiency.

124

125 There are further scientific motivations for speculating on the potential of observing Ganymede's  
126 H<sub>2</sub>O exosphere with JUICE. In particular, the observation of spectral emissions through limb  
127 scanning near Ganymede's poles, may provide information related to the preferential access of  
128 charged particles to the moon's polar caps furnishing important constraints for the surface weathering

129 history. The details of the ion access to Ganymede's surface, although attributed to the moon's  
130 magnetic field topology, have been long debated in the scientific community. Smith et al. (1979),  
131 based on Voyager observations, and Khurana et al. (2007), based on Galileo imaging (see figure 3 of  
132 their paper), explained the presence of observed bright polar caps on Ganymede with sputter-induced  
133 redistribution and subsequent cold trapping of water molecules, which result in a newer surface,  
134 continuously eroded. In particular, Khurana et al. (2007) pointed out a close correspondence between  
135 the open-closed magnetic field lines boundary and the boundary of the Ganymede's polar cap that  
136 they interpreted as evidence that the latter is associated with charged particle effects. Khurana et al.  
137 (2007) suggested also that the equatorial leading/trailing asymmetry (i.e., the albedo of the leading  
138 hemisphere is higher than the trailing one; Clark et al., 1986) was due to the preferential flux of ions  
139 onto Ganymede's leading hemisphere due to magnetotail reconnection, an hypothesis that was later  
140 confirmed by ion-trajectory simulations by Plainaki et al. (2015) and Fatemi et al. (2016). Numerical  
141 simulations of both energetic ion precipitation on Ganymede's surface and sputter-induced exosphere  
142 generation (e.g. Jia et al., 2009; Plainaki et al., 2015; Poppe et al., 2018) seem to support such a  
143 scenario, with respect to both aforementioned points. In particular, simulations by Plainaki et al.  
144 (2015) and Poppe et al. (2018) show a shielded region close to Ganymede (at distances  $< 1.5 R_G$ )  
145 asymmetrically displaced towards the sub-Jovian trailing hemisphere, with enhancements of lower-  
146 energy ion flux along the trailing-side boundaries of Ganymede's Alfvén wings. Moreover,  
147 enhancements in the flux on the anti-Jovian leading hemisphere are present (Poppe et al., 2018). It's  
148 worth noting, however, that current models depend significantly on a series of physical parameter  
149 assumptions which are currently poorly known, mainly due to the absence of an adequate quantity of  
150 in situ data and also because their quality in terms of spatial and spectral resolution hinder the  
151 inference of the necessary properties. Moreover, Ganymede has been mostly observed by ground-  
152 based telescopes so far and for this reason the spatial resolution and coverage of the currently  
153 available databases are rather limited. For example, the consideration in the models of the moon's  
154 magnetosphere morphology (see, for instance, the different approaches by Paty et al. 2008, Jia et al.

2009 and Fatemi et al. 2016), or the detailed composition of the icy surface (including impurities) has direct impacts in the modeled sputtering and sublimation rates of the surface. For this reason, and despite the numerous kinetic models proposed in literature, we do not have yet the necessary information to disentangle the influence of different mechanisms on the spectral properties of Ganymede's surface.

The spectral properties of the exosphere of Ganymede must be resolved for determining the properties of the space environment of Ganymede and for accurately mapping ion precipitation to the icy surface, a key mechanism linking the moon itself to the Jovian magnetospheric environment. In this paper, we investigate the possibility for MAJIS to observe spectral emission signatures of Ganymede's H<sub>2</sub>O exosphere, such as the non-Local Thermal Equilibrium (non-LTE) photon emissions from water molecules, using different modelled density profiles. First, we compare the existing models of Ganymede's water exosphere. We then use these model outputs to estimate the different scenarios for the expected IR emission from water molecules. In particular, in Section 2 we briefly review the generation mechanisms of Ganymede's H<sub>2</sub>O exosphere and discuss how the morphology of the neutral environment depends on the properties of the charged particle circulation around the planet. We also discuss the environment characteristics derived by different models. In Section 3 we present the main characteristics of the MAJIS instrument relevant for our investigation and we estimate the expected signal non-LTE photon emission from the water exospheric molecules. Endogenic processes can also contribute to exospheric density enhancements. In particular, ongoing cryovolcanic activity has been identified on Enceladus, and probably on Europa, through the observation of water (gas and ice) plumes (Porco et al., 2006; Sparks et al., 2017). Although no such evidence has been found so far for Ganymede, the JUICE mission offers a unique opportunity for searching for such an activity in geometric configurations not accessible from the Earth's orbit. In this regard, remote observations in visible and near-infrared spectral range at very high solar phase angle (or even in solar occultation geometry, if possible) are the most promising, since a plume



181 scatters solar light much more efficiently in the forward direction. In Section 4, we try to establish  
182 the potential observability of these phenomena with MAJIS, considering different observing study  
183 cases representative of different mission phases. In Section 5, we discuss the results of our  
184 calculations and present a summary of conclusions together with some future plans to optimize  
185 MAJIS observations.

186

## 187 **2. Generation of the water vapor exosphere of Ganymede**

188

### 189 *The role of Ganymede's mini magnetosphere*

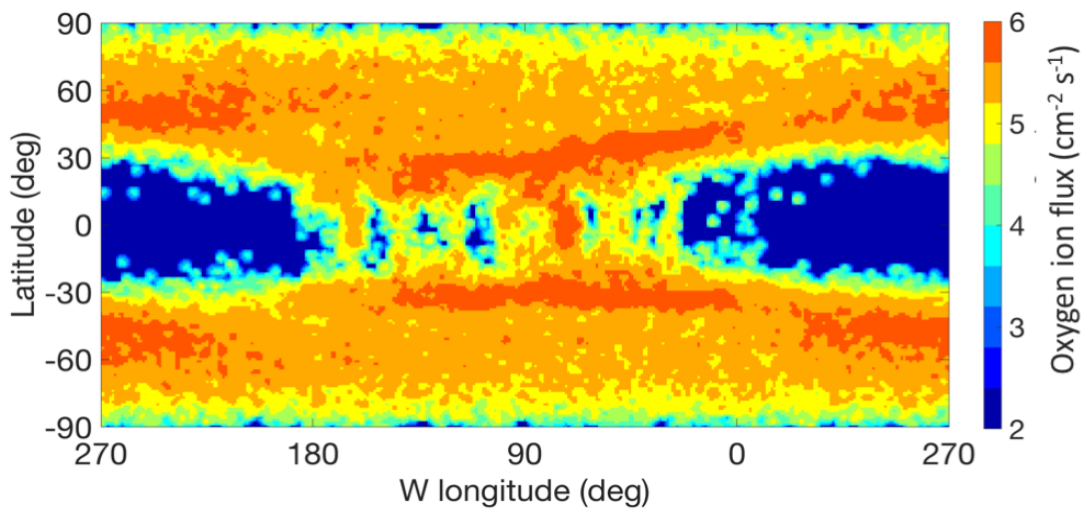
190 The plasma-surface interactions guided by Ganymede's intrinsic magnetic field are the main drivers  
191 of the H<sub>2</sub>O exosphere generation. The major plasma source in Jupiter's magnetosphere is the  
192 volcanic-active moon Io which ejects material that becomes dissociated and/or ionized by the solar  
193 EUV radiation (Broadfoot et al., 1979), generating predominantly multiply charged Oxygen and  
194 Sulfur ions (Bagenal et al. 1996). At Ganymede's distance from Jupiter, the plasma is confined to a  
195 low scale height current sheet (also called Jupiter's Plasma Sheet - JPS) cantered roughly around the  
196 Jovian magnetic equator (Khurana et al., 2004; 2007). Because of the 10° tilt of Jupiter's magnetic  
197 field to the planet's rotational axis, the current sheet oscillates up and down Ganymede's orbital plane.  
198 Within the plasma sheet and up to a distance of  $\sim 10 R_J$  from Jupiter, the plasma slightly subcorotates  
199 at  $v \sim 150$  km/s, whereas at the distance of Ganymede (at about  $15.3 R_J$  from Jupiter) it lags the  
200 corotation, in the azimuthal direction, by 37 km/s (Kivelson et al., 2004). At Ganymede, the Jovian  
201 magnetospheric plasma is characterized by a thermal component with density,  $n_e, \sim 5\text{--}20 \text{ cm}^{-3}$ , and  
202 temperature,  $T_e, \sim 20$  eV plus a suprathermal component with  $n_e \sim 0.5\text{--}2 \text{ cm}^{-3}$ ,  $T_e \sim 2 \text{ keV}$  (Scudder et  
203 al., 1981). The bombardment of Ganymede's surface by high energy ions induces radiolysis and  
204 direct sputtering of surface molecules that populate the moon's exosphere (Cassidy et al., 2013). The  
205 generation and evolution of the exosphere of an icy moon is a complex process that depends on the  
206 environment properties (e.g. spectrum and flux spatial distribution of Jupiter's magnetospheric ion

207 population), the characteristics of the moon's surface (e.g. composition, impurities, temperature), as  
208 well as the moon's orbital phase around Jupiter (see, for instance, Plainaki et al., 2013; Leblanc et al.,  
209 2017). There is a widespread consensus that Jupiter's energetic ion environment provides the major  
210 contribution to the generation of Ganymede's exosphere although some alternative scenarios, such  
211 as secondary sputtering by ionospheric ions or water sublimation, cannot be excluded. Locally, in  
212 regions near the subsolar point, where the maximum diurnal temperatures are reached (up to 152 K;  
213 Orton et al., 1996) sublimated water is believed to be the dominant exosphere component. Several  
214 modelling efforts have advanced our understanding of the generation of Ganymede's exosphere  
215 providing important constraints for the involved processes. As in the Europa case, exospheric models  
216 are based on very different approaches employing a variety of parameters and assumptions that result  
217 in a large range of values for the obtained outputs. For a general description and comparison of the  
218 available techniques for studying the exospheres of the Galilean satellites see the works by Marconi  
219 (2007), Shematovich (2016), Plainaki et al. (2018) and references therein.

220  
221 Since the role of the moon's bombardment by energetic ions is crucial for the generation of the  
222 sputter-induced H<sub>2</sub>O exosphere, significant effort has been devoted to simulating the ion circulation  
223 around Ganymede and precipitation to the surface. Some of the models do provide maps of the  
224 precipitation of plasma and charged energetic particles to the moon's surface as well as estimates of  
225 sputtering rates. For instance, Paranicas et al. (1999) assumed that sputtering takes place in the polar  
226 caps, which they defined as the surface area above the latitude of  $\pm 45^\circ$ , and they estimated a total rate  
227 of  $2 \cdot 10^{26} \text{ s}^{-1}$ . The electric and magnetic fields determining the charged particle trajectories differ  
228 among different magnetospheric models considered in literature (see, for example, Jia et al. 2009,  
229 Fatemi et al. 2016, and references therein). Cooper et al. (2001) performed a back tracing technique  
230 to simulate ion circulation within Ganymede's magnetosphere with only superimposed magnetic  
231 fields based on Galileo data from the G2 flyby; the total sputtering rate estimated by these authors  
232 was  $\sim 4.3 \cdot 10^{26} \text{ s}^{-1}$ .

233 Plainaki et al. (2015) used the electric and magnetic fields from the Jia et al. (2009) global  
 234 Magnetohydrodynamic (MHD) model of Ganymede's magnetosphere to trace energetic charged  
 235 particle trajectories around the moon and to identify the regions where ions hit the ice activating  
 236 particle release through sputtering and radiolysis. In particular, three singly charged energetic species  
 237 ( $H^+$ ,  $O^+$ , and  $S^+$ ) at a selection of discrete energies ranging between 1 and 100 keV, were considered.  
 238 To absolutely normalize the flux of incident energetic particles, they used the distributions for each  
 239 species as determined by Paranicas et al. (1999). For each specific pair of ion composition and energy,  
 240  $10^8$  particles were simulated to ensure sufficient statistics. The total  $O^+$  precipitating flux integrated  
 241 in energy in the simulation by Plainaki et al. (2015) is shown in Figure 1. The total  $H_2O$  sputtering  
 242 rate estimated by Plainaki et al. (2015) was  $7 \cdot 10^{25} s^{-1}$ . Recently, Poppe et al. (2018) developed a  
 243 backwards ion tracing model to define the energetic ion population characteristics in the near-  
 244 Ganymede space. They used the three-dimensional, self-consistent hybrid model simulations of  
 245 Ganymede's magnetospheric interaction with the Jovian magnetosphere by Fatemi et al. (2016) to  
 246 obtain the electric and magnetic field needed for their single-particle simulations. In the simulations  
 247 by Poppe et al. (2018) three energetic species,  $H^+$ ,  $O^{++}$ , and  $S^{+++}$ , at three discrete energies, 30 keV,  
 248 300 keV, and 3 MeV were considered. We note that the MHD model by Jia et al. (2009) is single-  
 249 fluid ( $O^+$ ) whereas Fatemi et al. (2016) have implemented a hybrid plasma model (kinetic ions and  
 250 fluid electrons) using only the thermal component (i.e., non energetic particles). Although the  
 251 simulations by Plainaki et al. and Poppe et al. did not consider exactly the same inputs (e.g. ion energy  
 252 spectrum; magnetic field model), the results of their simulations are generally in good agreement.  
 253 Both studies show that there is a decrease in the ion flux from the upstream boundary at a distance of  
 254  $\sim 2 R_G$  approaching the moon. Moreover, there is a shielding from the ions region on the surface  
 255 within the distance of  $\sim 2 R_G$  from Ganymede's center, where  $R_G$  is Ganymede's radius. The exact  
 256 dimension of this shielded region depends on the magnetic rigidity of the ions considered (higher  
 257 rigidity ions have access on the surface at lower latitudes). Enhancements in the energetic ion flux  
 258 downstream of Ganymede were also found by both models. Both the simulations by Plainaki et al.

259 (2015) and Poppe et al. (2018) showed enhancements extending vertically along the upstream  
 260 boundaries of the Alfvén wings, however the morphologies of the flux distribution are not identical;  
 261 indeed, the magnetic field model considered in each case determines the details of the deceleration  
 262 process of the incident ion flux upon entering the Alfvén wings and the deflection of incident  
 263 trajectories from the near-equatorial plane to the polar regions. Over Ganymede’s polar caps the flux  
 264 is diminished whereas downstream both simulations show evidence of trapped populations and a  
 265 reconnection region within Ganymede’s magnetotail at distances between 2 and 4  $R_G$ .



266  
 267 **Figure 1:** Integral  $O^+$  flux (in  $\text{cm}^{-2} \text{s}^{-1}$ ) precipitating at Ganymede’s surface based on simulations by  
 268 Plainaki et al. (2015) considering an ion energy range from 1 keV to 100 keV. In the coordinate  
 269 system used in this plot, the leading hemisphere apex is at longitude  $90^\circ$  and the sub-Jovian point at  
 270 longitude  $0^\circ$ . The MHD model used for the simulations considers conditions similar to those during  
 271 the Galileo G8 flyby (Ganymede was near the center of Jupiter’s plasma sheet).

## 272 273 *Exosphere models*

274 Moon exospheres have been discussed many times in the past, also through a comparative  
 275 planetology approach (see, for example, the collection of papers published by Coustenis et al. (2010)).  
 276 Our knowledge on the configuration of Ganymede’s  $H_2O$  vapor exosphere is currently largely based  
 277 on modelling efforts. Exospheric models are in general based on very different approaches (e.g., the

278 assumption of a collisional or a collisionless environment) and usually include H<sub>2</sub>O and other  
279 exospheric species as well.

280

281 The 2-D axisymmetric Direct Simulation Monte Carlo (DSMC) model by Marconi (2007) used a  
282 multispecies approach to derive the atmospheric O<sub>2</sub>, H<sub>2</sub>O, H<sub>2</sub>, and H, O, and OH spatial structure,  
283 considering the non-uniform distribution of the surface temperature based on the PLS measurements  
284 by Galileo. Marconi (2007) found that near the subsolar point the dominant component is H<sub>2</sub>O vapor,  
285 whereas near the polar regions the main component, at low altitudes, is molecular Oxygen; the  
286 uppermost layers of the exosphere are populated by molecular hydrogen according to this model. A  
287 similar approach was also followed by Shematovich (2016) who showed that collisions are  
288 responsible for the observed H<sub>2</sub>O and O<sub>2</sub> concentration at altitudes between 10 and 100 km from the  
289 surface.

290

291 Ganymede's exosphere has been studied also through 3-D test-particle models (e.g. Turc et al., 2014;  
292 Plainaki et al., 2015). Turc et al. (2014) assumed a collisionless 3-D model approach for simulating  
293 Ganymede's exosphere above the sunlit trailing hemisphere. The Lyman- $\alpha$  emission brightness  
294 obtained based on the model by Turc et al. (2014) was found much smaller than the one observed by  
295 Barth et al. (1996). The modelled exosphere is clearly structured by the two particle surface sources,  
296 sputtering and sublimation, resulting in a strong dichotomy between the subsolar region, where  
297 sublimation takes place, and the rest of the exosphere. Far away from the subsolar region, O<sub>2</sub> is  
298 accumulated close to the surface; instead, the lighter H<sub>2</sub> is found at higher altitudes, even above the  
299 subsolar region.

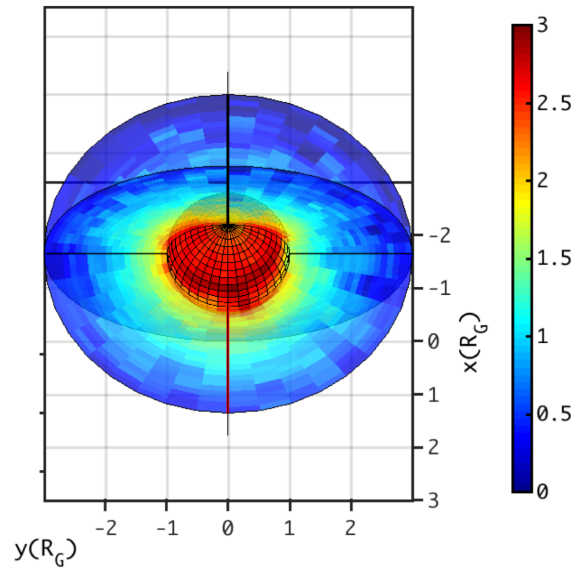
300

301 The model by Plainaki et al. (2015) was the first one to take into account the effect in the exosphere  
302 generation of the ion precipitation to the moon's icy surface. This 3-D single-particle Monte Carlo  
303 model was based on the previously released Europa Global model of Outgoing exospheric neutrals

(EGEON, Plainaki et al. 2010;2012; 2013) as well as previous efforts for simulating Mercury's  
 exosphere (Mura et al., 2009). Plainaki et al. (2015) assumed that the main sources of Ganymede's  
 neutral environment are ion sputtering, radiolysis and water ice sublimation. The EGEON code takes  
 into account the exact angle of incidence for the ions impacting the surface. It was shown that the  
 morphology of the exosphere is significantly determined by the aforementioned processes and,  
 moreover, for the sputtered-H<sub>2</sub>O case, there is a large difference in the concentrations of neutral  
 components between the high and low latitude regions of the exosphere. Figure 2 shows the density  
 spatial distribution of Ganymede's sputtered-H<sub>2</sub>O exosphere according to the EGEON model.  
 Moreover, Plainaki et al. (2015) considered H<sub>2</sub>O-sputtering yields depending on the incident ion  
 energies and therefore their exospheric model, contrary to previous ones, was based on a sputtering  
 efficiency that was spatially variable. Loss processes have also an important role in the exosphere  
 spatial distribution. Plainaki et al. (2015) incorporated in their model different plasma-induced loss  
 processes (see their table 4) among which charge exchange between low-energy charged particles  
 and exospheric molecules. Atmospheric sputtering can be an important sink for planetary and lunar  
 neutral environments, as discussed in detail by Johnson (1994), depending on the relative bulk motion  
 between plasma and neutral particles (see also discussion in Plainaki et al. (2015) and references  
 therein). In EGEON, the estimated loss rate of Ganymede's H<sub>2</sub>O exosphere due to charge exchange  
 is of the order of  $\sim 10^{-5} \text{ s}^{-1}$ . The importance of this process was highlighted also for the Europa case  
 in the studies by Saur et al. (1998), Dols et al. (2016) and Lucchetti et al. (2016). Plainaki et al. (2015)  
 showed that the spatial distribution of the sputtered H<sub>2</sub>O molecules reflects the characteristics of the  
 interaction between Ganymede and Jupiter's magnetospheric particles. In particular, in the full-  
 mirroring approximation for the ion precipitation pattern, it was shown that the H<sub>2</sub>O exosphere is  
 efficiently sputtered both in the polar region and the low latitude wake hemisphere. We note here that  
 both studies by Marconi (2007) and Plainaki et al. (2015) argue that the neutral environment is largely  
 collisionless, except for a small region near the subsolar point.

330 Recently, Leblanc et al. (2017) studied Ganymede's neutral environment taking into account Jupiter's  
331 gravitational influence and the evolution of the exosphere along the moon's orbit around the giant  
332 planet. Their 3-D Monte Carlo model considered water sublimation and sputtering as the main  
333 exosphere sources, and electron impact ionization and dissociation as well as particle-surface  
334 interactions, as loss processes. The model follows the dynamical evolution of the exosphere as  
335 Ganymede orbits Jupiter. The neutral species considered in this model were O<sub>2</sub>, O, H<sub>2</sub>O, H, H<sub>2</sub>, and  
336 OH released after the surface bombardment by incident Jovian ions. The model by Leblanc et al.  
337 (2017) assumed that Jovian ions precipitate to the surface within the open field line regions. In  
338 particular, the model considered the open-closed magnetic field lines boundary (OCFB) as derived  
339 by the auroral observations described in McGrath et al. (2013). According to these authors, the  
340 Ganymede exosphere appears to be highly stratified in density and composition due to the variation  
341 of the ejection mechanisms and motion of the ejected molecules over the moon's orbital period. The  
342 fate of the ejecta is also species-dependent due to the species dependent surface interactions. Leblanc  
343 et al. (2017) confirmed the difficulty in providing a precise estimation of the water sublimation being  
344 this process very sensitive in temperature variations and surface composition properties. Last, they  
345 argued that the consideration of collisions among the particles in Ganymede's exosphere has a minor  
346 effect in the density distribution. In Table 1 we summarize the assumptions and main findings of  
347 current models of Ganymede's H<sub>2</sub>O exosphere.

348



349

350 **Figure 2:** Density spatial distribution of Ganymede's sputtered-H<sub>2</sub>O exosphere according to the  
 351 model by Plainaki et al. (2015), as seen from the north, at a viewing angle between 0° and 90° with  
 352 respect to the equator. The scale is logarithmic and density is measured in particles/cm<sup>3</sup>. To calculate  
 353 the ion surface precipitation pattern, a necessary input for EGEON, the full-mirroring approximation  
 354 has been considered (for details see Plainaki et al. 2015). H<sub>2</sub>O is efficiently sputtered in the polar  
 355 regions as well as in the low latitude wake hemisphere (leading hemisphere). In the coordinate system  
 356 used in this plot, the orbital direction is along the positive x axis whereas Jupiter is towards the  
 357 positive y axis.

358

359 **Table 1:** Ganymede's H<sub>2</sub>O exosphere: comparison of model assumptions and main findings

H <sub>2</sub> O- exosphere model	Ion –surface interaction morphology	Technical characteristics Notes	H <sub>2</sub> O release rate at the surface	Exosphere scale-height
Marconi (2007)	N/A	DSMC model	sputtering: $1.5 \times 10^{26} \text{ s}^{-1}$  sublimation: $7 \times 10^{29} \text{ s}^{-1}$	70 km



Shematovich (2016)	N/A	DSMC model	sputtering: $1.6 \times 10^{26} \text{ s}^{-1}$ (Cooper et al. 2001)  sublimation: as in Marconi (2007)	80 km
Turc et al. (2014)	guided by field lines that are assumed to be closed at latitudes below $\pm 45^\circ$ and open above the polar regions	collisionless single- particle Monte Carlo model	sputtering: $1.5 \times 10^{26} \text{ s}^{-1}$  sublimation: as in Marconi (2007)	65 km
Plainaki et al. (2015)	guided by the MHD-model by Jia et al. (2009); ion circulation simulations have been performed	collisionless single- particle Monte Carlo model  ion circulation simulations are used as an input for the estimation of the exosphere	sputtering: $7 \times 10^{25} \text{ s}^{-1}$ (estimated within the model assuming the Famà et al. (2009) yields and ion spectrum by Paranicas et al. (1999))  sublimation: as in Marconi (2007)	55 km
Leblanc et al. (2017)	taking place at the regions of the open field lines as defined by the McGrath	collisional Monte Carlo model  consideration of the dynamical evolution	sputtering: $8 \times 10^{27} \text{ s}^{-1}$ sublimation: $8 \times 10^{21} \text{ s}^{-1}$ (low sublimation scenario)	$\sim 400 \text{ km}$

	et al. (2013) auroral observations	of the exosphere along the moon's orbit		
--	--	---	--	--

360

361 Figure 3 presents a comparison between the H<sub>2</sub>O density profiles calculated by different models. We  
362 note that around the subsolar point and up to an altitude of at least ~250 km, all models have the same  
363 trend, with the exception of the model by Leblanc et al. (2017), where low sublimation rate is  
364 considered ab initio. We note that the consideration by Leblanc et al. of a low sublimation rate was  
365 motivated by the matching of the observed ratio of the H<sub>2</sub>O column density between the leading and  
366 trailing hemispheres (Hartogh et al., 2013). All models agree that the environment is collisional only  
367 locally, i.e. near the subsolar point, assuming that the underlying surface region is mainly composed  
368 from ice. The Marconi (2007), Plainaki et al. (2015) and Turc et al. (2014) models agree that the  
369 maximum H<sub>2</sub>O density above the subsolar surface region is of the order of  $10^9 \text{ cm}^{-3}$ , whereas for the  
370 model by Shematovich (2016) the peak density is  $\sim 10^8 \text{ cm}^{-3}$ . Models begin to diverge substantially  
371 at higher altitudes (above ~200 km). In that region, the density of the sublimated exosphere is  
372 significantly decreased, as shown in the collisionless model by Plainaki et al. (2015) hence any  
373 diversion of a model from a strictly thermal profile is likely the result of either the assumed chemistry  
374 taking place within the exosphere or of the assumed initial energy distribution upon the particle  
375 release from the surface.

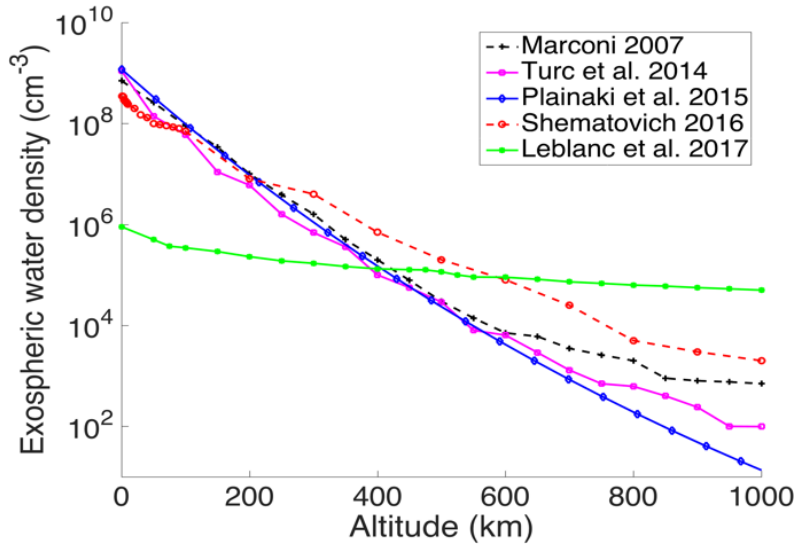


**Figure 3:** H<sub>2</sub>O density profiles of Ganymede's exosphere above the subsolar point, as estimated by different models.

### 3. Detecting Ganymede's water vapor exosphere with JUICE/MAJIS

The ESA JUICE mission (Grasset et al., 2013), whose launch is scheduled in 2022, will explore the icy Galilean satellites thanks to a series of flybys of Callisto, Ganymede and Europa, prior to finally entering orbit around Ganymede, the mission's main target. The Ganymede dedicated orbit is divided into a high altitude (~5000 km) circular orbit phase (GCO-5000), including two elliptical orbit sub-phases, expected to last about 120 days, and a medium altitude (~500 km) circular orbit (GCO-500) phase, at least 150 days long. During periods in between flybys, observation time will be devoted also to the study of Jupiter's atmosphere, magnetosphere and auroras. The investigation of Ganymede's exosphere through the analysis of hyperspectral VIS-IR data is among the science objectives of MAJIS. In particular, MAJIS will investigate the non-LTE exospheric emissions by observing the satellite's limb at different locations and geometries, so as to assess the abundance of the exospheric component. A brief example of possible science investigations with JUICE related to

the icy satellite exospheres has been recently proposed by Plainaki et al. (2018; see paper's Section 4).

The MAJIS experiment onboard JUICE is led by a French-Italian consortium (Langevin et al., 2018; Piccioni et al., 2014). MAJIS is a compact visible and near-infrared imaging spectrometer covering the spectral range from 0.5 to 5.54  $\mu\text{m}$ , split in two channels (Piccioni et al., 2019; Guerri et al., 2018). The VIS-NIR spectral channel covers the 0.5-2.35  $\mu\text{m}$  band with an average sampling of 3.66 nm/band. The IR channel works in the 2.25-5.54  $\mu\text{m}$  range with a 6.51 nm/band average sampling. The optical design of the MAJIS instrument relies on a f/3.2 aperture Three Mirrors Anastigmatic (TMA) telescope (pupil equivalent diameter is 75 mm; focal length is 240 mm), matching two camera imaging spectrometers, sharing the same entrance slit by means of a collimator. A dichroic element is used to split the light beam between the two spectral channels (VIS-NIR and IR). The operative temperature of the Optical Head ( $<140\text{ K}$ ) and the cryogenic IR detector temperature ( $<90\text{ K}$ ) are achieved through passive cooling. Two detectors with similar format are foreseen for both spectrometers comprising an array of  $800 \times 1016$  pixels. Binning by 2 will always be applied in the spatial direction (400 pixels). Binning by 2 is also nominal in the spectral direction (508 spectral elements), leading to a 36  $\mu\text{m}$  pitch, but up to 264 spectral bands can be acquired without spectral binning, leading to a frame  $400\text{ pixels} \times 640\text{ spectral element}$ . The resulting Instantaneous Field of View (IFOV) is 150  $\mu\text{rad}$ , while the MAJIS FOV along the slit is  $\pm 1.7^\circ$ . The IFOV size corresponds to resolutions of 75 m/px and 300 m/px when observing respectively at nadir and at limb from a 500 km circular orbit around Ganymede. The instrument has a high operational flexibility thanks to a series of technical capabilities. A steerable mirror in the telescope allows MAJIS to acquire bidimensional hyperspectral images through consecutive scans and to compensate for the spacecraft motion during the GCO-500 orbital phase or during flybys. A series of different operational modes have been pre-set allowing spatial and spectral binning. Radiation noise due to charged particle populations can be reduced through a despiking algorithm based on sub-frame sorting and summing,

also useful to increase the on-board data compression rate for effectively reducing the data downlink volume (Langevin, 2018). Spatial and spectral binning beyond the nominal level (36  $\mu\text{m}$  pitch) will be implemented in order to optimize the data volume when providing extensive spatial coverage of the icy satellites at medium resolution (1 to 5 km/pixel) as well as time evolution sequences for the atmosphere of Jupiter and the exospheres of satellites. In Table 2, the most significant characteristics of MAJIS are summarized, while more details can be found in Guerri et al. (2018) and Piccioni et al. (2019).

Apart from the search for possible plumes (which will be discussed in the next section), the MAJIS limb measurements are relevant to the search for  $\text{H}_2\text{O}$  exospheric emission. The most favorable observing condition in this case is when the Line Of Sight (LOS) within the exosphere is totally illuminated. In this case, due to effective radiative pumping, a non-LTE photon emission signal from water vapor will be occurring and can in principle be strong enough to be revealed by MAJIS. In particular, the MAJIS spectral range covers the  $\text{H}_2\text{O}$  non-LTE emission bands between 2.4 and 3  $\mu\text{m}$ . The  $\nu_3$   $\text{H}_2\text{O}$  band at 2.67  $\mu\text{m}$  is the strongest one in this spectral range and we expect to observe it together with the  $\nu_1$  and  $\nu_2$   $\text{H}_2\text{O}$  bands. Since Ganymede's exosphere is as optically thin as the cometary atmospheres, we expect fluorescence to be the main excitation mechanism for the  $\text{H}_2\text{O}$  bands (Crovisier, 1987; Bockelée-Morvan, 1987; Bockelée-Morvan et al., 2004). To estimate, therefore, the non-LTE radiance to be measured from a spectrometer on board a spacecraft in limb viewing, we follow the approach suggested by Bockelée-Morvan et al. (2015) and Villanueva et al. (2012). That being the case, we are able to obtain a first simulation of the MAJIS observations of Ganymede's  $\text{H}_2\text{O}$  exosphere. In this exercise, we consider currently available  $\text{H}_2\text{O}$  exosphere models (see previous section) together with the instrument performance parameters. In this paper, we do not perform estimations corresponding to the sublimated water density estimated by Leblanc et al. (2017). The sublimation rate assumed by these authors is significantly lower than the ones considered by the other models resulting in a significantly reduced Signal-to-Noise Ratio (SNR). The assumption of

20

such a low sublimation rate has its origin to the matching of the observed ratio of the H<sub>2</sub>O column density at the leading and trailing hemispheres (Hartogh et al., 2013), nevertheless, since the methodology for deriving this quantity and the related uncertainty in the estimation are not yet clear we prefer to take into account only the sublimation rate estimations available in published literature. The estimations presented here are likely to be reviewed in the next years also due to theoretical model updates hence the scope of this paper is to provide an indicative range for the expected exospheric measurements.

452

453

454

**Table 2:** Basic technical characteristics of MAJIS. For a detailed description of the instrument the reader is referred to Guerri et al. (2018) and Piccioni et al. (2019).

457

Basic technical characteristics of MAJIS	
Spectral range	0.5 - 5.54 $\mu\text{m}$ <i>VIS-NIR channel:</i> 0.5-2.35 $\mu\text{m}$ <i>IR channel:</i> 2.25-5.54 $\mu\text{m}$
Spectral sampling	<i>VIS-NIR channel</i> 3.66 nm/band <i>IR channel:</i> 6.51 nm/band
FOV along the slit	$\pm 1.7^\circ$
IFOV	150 $\mu\text{rad}$
OH operative temperature	110 - 160 K
VIS-NIR detector operative temperature	130 K (nominal)
IR detector operative temperature	90 K (nominal)

458

459

460 To estimate the expected non-LTE radiance we extract the line parameters from the HITRAN  
 461 database (Gordon et al., 2017) and we compute the cross-sections  $\sigma$  (in  $\text{cm}^2$ ) for the roto-vibrational  
 462 lines of the  $\nu_1$ ,  $\nu_2$  and  $\nu_3$   $\text{H}_2\text{O}$  band. We assume band emission rates (g-factors),  $gf$ , equal to  $3.349 \times$   
 463  $10^{-4} \text{ s}^{-1}$ ,  $3.33 \times 10^{-5} \text{ s}^{-1}$  and  $2.67 \times 10^{-4} \text{ s}^{-1}$  for the  $\text{H}_2\text{O}$   $\nu_3$ ,  $\nu_1$  and  $\nu_2$  bands, respectively (Villanueva  
 464 et al., 2012). Since the aforementioned values refer to at the heliocentric distance of 1 AU, their  
 465 rescaling to 5.2 AU, is required.

466 The band integrated radiance (in  $\text{W m}^{-2} \text{ sr}^{-1}$ ) can be estimated as follows:

467

$$468 \quad I_{i,l} = \frac{(h \cdot \underline{\nu})}{(4 \cdot \pi)} \cdot gf_i \cdot N_l \quad (1)$$

469 where  $\underline{\nu}$  is the central frequency of the band,  $h$  is the Planck constant,  $N_l$  (in  $\text{m}^{-2}$ ) is the column density  
 470 along the LOS inside the  $l$  exospheric level. The  $i$  index characterizes the  $\text{H}_2\text{O}$  spectroscopic  
 471 transition. Since the band integrated radiance can be also written as

$$472 \quad I_{i,l} = f_{i,l} \cdot \int \sigma_{i,l}(\nu) d\nu \quad (2)$$

473 where  $f_{i,l}$  is a conversion parameter (in  $\text{W cm}^{-4} \text{ cm sr}^{-1}$ ), based on Eq.s. (1) and (2), the emitted  
 474 radiance  $R_{i,l}$  (in  $\text{W m}^{-2} \text{ cm sr}^{-1}$ ) along the LOS inside the  $l$  exospheric level and for the  $i$  transition can  
 475 be written as

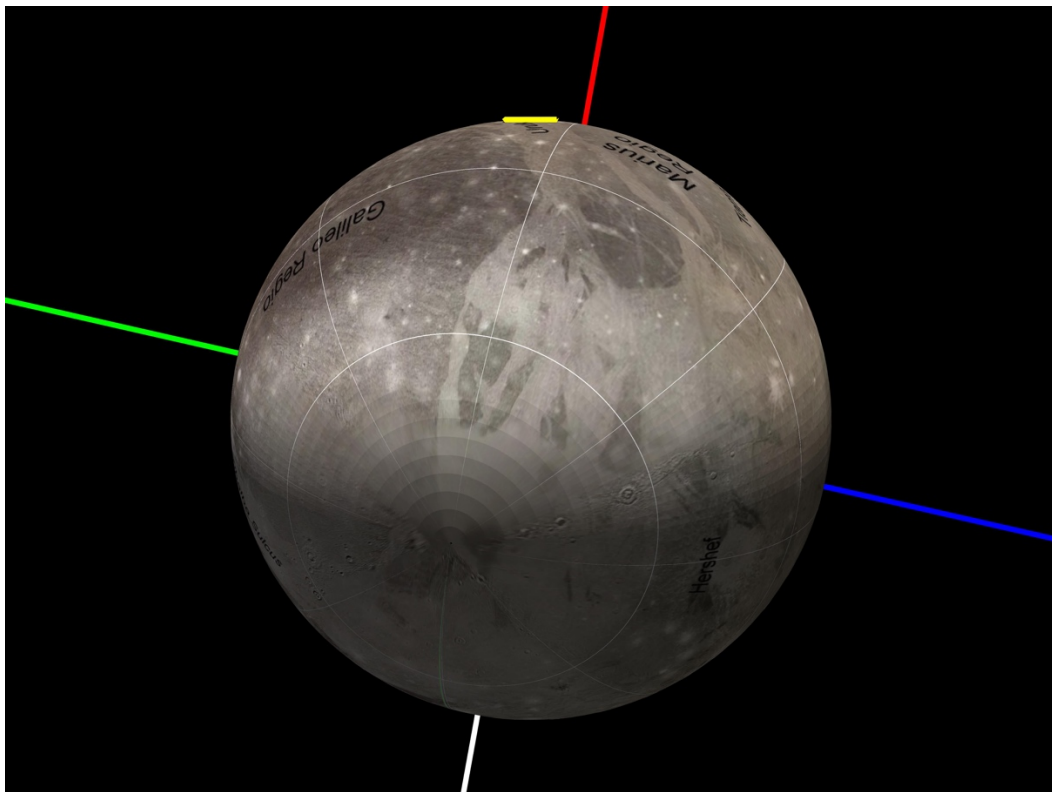
$$476 \quad R_{i,l}(\nu) = f_{i,l} \cdot \sigma_{i,l}(\nu) = \frac{h \cdot \nu \cdot gf_i \cdot N_l}{4 \cdot \pi \cdot \int \sigma_{i,l}(\nu) d\nu} \cdot 10^4 \quad (3)$$

477 Considering all the spectroscopic transitions and exospheric levels occurring along the LOS, the  
 478 radiance at the detector is:

$$479 \quad R(\nu) = \sum_i \sum_l R_{i,l}(\nu) \quad (4)$$

480 The radiance  $R$  computed so far has a very high spectral resolution equal to  $2 \times 10^{-3} \text{ cm}^{-1}$  chosen as the  
 481 best compromise between the inclusion of the spectroscopic lines and the required computational  
 482 time. We then convolve  $R$  with the MAJIS IR channel instrumental line shape expected to follow a

483 Gaussian profile with a conservative Full-Width-Half-Maximum FWHM estimated at 12.98 nm  
 484 corresponding to a factor of two times the spectral sampling of 6.49 nm (Guerri et al., 2018).  
 485  
 486 During Ganymede flybys as well as in Ganymede orbits, all exosphere observations are planned with  
 487 the slit oriented parallel to the limb. This is the best configuration as the whole slit would be exposed  
 488 to the maximum exosphere signal while reducing possible straylight from the surface, and the  
 489 sensitivity of the measurement to the tangent altitude would be maximum as well. In Figure 4 we  
 490 show the geometry of a hypothetical observation taking place at UTC 2032-09-15 T09:42:42, with  
 491 JUICE being distant  $\sim 7700$  km from the center of Ganymede (altitude of 5100 km), with a spatial  
 492 resolution of  $\sim 0.75$  km at the sub-spacecraft point and  $\sim 1$  km in terms of altitude resolution of the  
 493 exosphere at the limb.



494  
 495  
 496 **Figure 4:** Observation of Ganymede exosphere on 2032-09-15 T09:42:42 in CREMA 3.0 with limb  
 497 pointing by MAJIS and the MAJIS slit oriented parallel to the limb. MAJIS FoV is the yellow



498 segment. Colored lines indicate directions towards Jupiter (white), anti-Jupiter (red), leading (green)  
499 and trailing hemisphere (blue). This attitude is a preliminary estimation: technical constraints such as  
500 solar illumination on panels are still to be evaluated.

501

502 Most exospheric observations during Ganymede flybys will be made at relatively large distances  
503 (e.g., 40000 km corresponding to a spatial resolution of 6 km/px) as closer observations conflict with  
504 remote sensing and geophysics observations of Ganymede. The most favorable phase for Ganymede  
505 exospheric observations is the near circular phase of GCO-5000 (120 days-long) and the two adjacent  
506 elliptical phases (2 x 15 days) as all latitudes can be observed in the optimum geometry (limb pointing  
507 with the MAJIS slit parallel to the limb) on orbital segments extending from the night side up to the  
508 pole. In this case pointing can be driven by exospheric observations whereas most remote sensing  
509 observations of the surface will be made on the day side of the GCO-5000 orbit. When the spacecraft  
510 is at an altitude of  $\sim 5000$  km the spatial resolution when pointing at the limb is 1.07 km/px. The  
511 dwell time is  $\sim 1$  s as the orbital velocity is 1.1 km/s. Such integration times lead to relatively low  
512 SNR. SNR can be improved by extending the repetition time at the expense of vertical spatial  
513 resolution. As the MAJIS slit is tangent to the limb, one can co-add spatial pixels without degrading  
514 the vertical spatial resolution at the center of the slit (closest to the limb). Since the co-adding  
515 technique involves only adjacent bins along the slit, which is oriented tangent to the limb, the worst  
516 binned spatial resolution is  $\sim 17$  km/px. We note that the considered exospheric model has a horizontal  
517 spatial resolution of about  $1/10 R_G$ , which is much higher than the worst spatial resolution we can  
518 have along the slit. Therefore, we can assume our exospheric conditions as homogeneous within the  
519 co-added bin. Moreover, during the other planned JUICE orbital phases around Ganymede (e.g.,  
520 GCO-500), the distance of the spacecraft from the target will be lower than the one we considered  
521 here and this will further improve the MAJIS spatial resolution with respect to the fixed horizontal  
522 spatial resolution of current exospheric models.

523

524 The noise level is estimated using the MAJIS radiometric model, taking into account the repetition  
525 time and the despiking strategy (sub-integration time and number of selected sub-integrations after  
526 sorting). An example of the signal we expect to measure between 2.4 and 3  $\mu\text{m}$  (the spectroscopic  
527 range with stronger  $\text{H}_2\text{O}$  line intensities) is shown in Figure 5. These simulations, based on the  
528 Plainaki et al. (2015) model extended in altitude up to 1000 km, are performed at a tangent latitude  
529 of  $\sim 10^\circ\text{N}$ , assuming the LOS within the exosphere totally illuminated. For completeness, we also  
530 estimated the SNR corresponding to the exospheric models of Marconi (2007; Figure A1),  
531 Shematovich et al. (2016; Figure A2), and Turc et al. (2014; Figure A3) which are presented in the  
532 appendix.

533 Two representative observation cases have been considered for observations from GCO-5000:

- 534 - High vertical resolution: 1.1 s repetition time, binning x 4 along the slit (projected IFOV: 1.1  
535 km vertical, 4.3 km along slit); despiking strategy: lowest of 3 CDS with 0.1 s integration  
536 time.
- 537 - Low vertical resolution: 9 s repetition time, binning x 16 along the slit (projected IFOV: 10  
538 km vertical, 17 km along slit); despiking strategy: average of 3 lowest CDS out of 6 with  
539 0.643 s integration time.

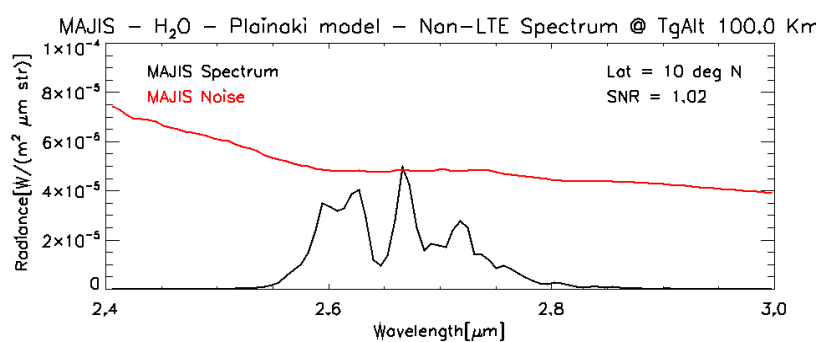
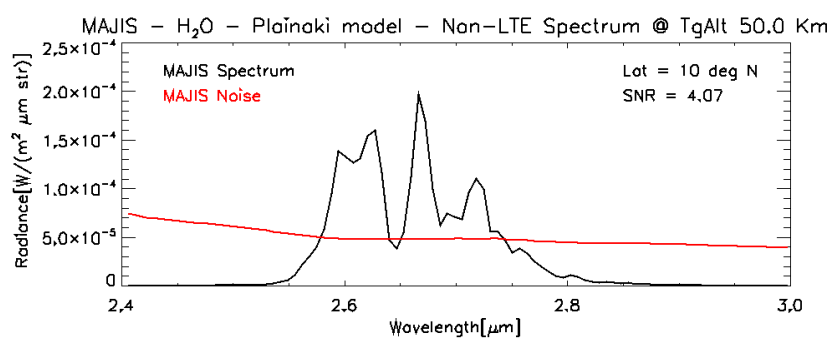
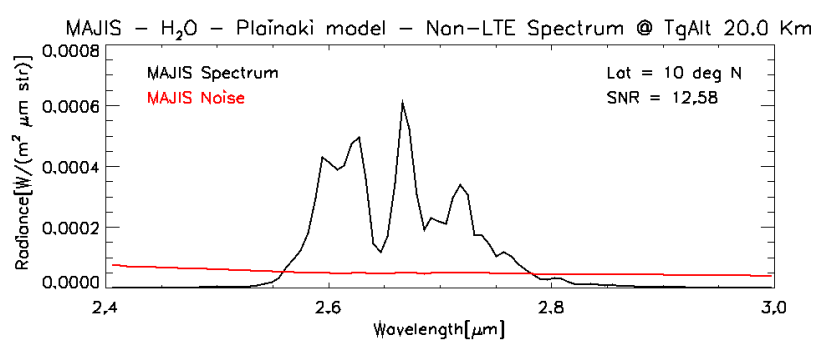
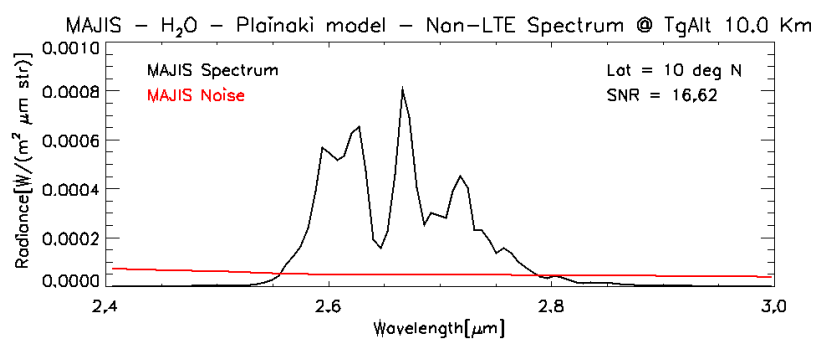
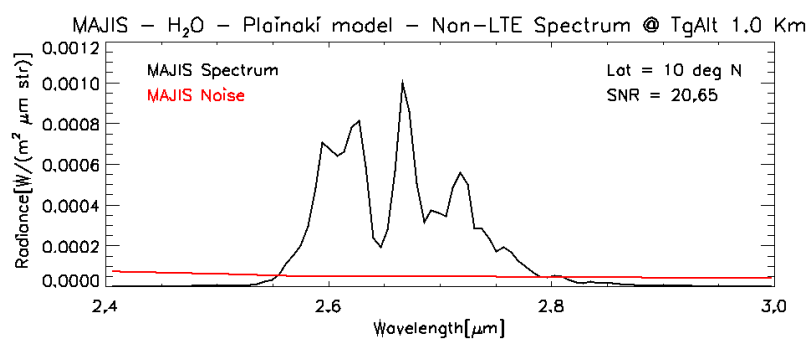
540 The estimated SNR at peak intensities have been evaluated in Table 3 for both observational modes  
541 at latitude  $\sim 10^\circ\text{N}$  and three tangent altitudes (10 km, 50 km and 100 km). Such observations will  
542 provide constraints on actual  $\text{H}_2\text{O}$  column densities as a function of altitude, making it possible to  
543 adjust the observation strategy for exospheres once in Ganymede orbit.

544

545 **Table 3:** Observing the water exosphere of Ganymede with MAJIS. The Signal-to-Noise Ratio (SNR)  
546 has been evaluated for high vertical resolution observations (spatial resolution 4.3 km along slit x 1.1  
547 km vertical) and low vertical resolution (17 km along slit x 10 km vertical) as a function of the tangent  
548 altitude for different  $\text{H}_2\text{O}$  exospheric models.

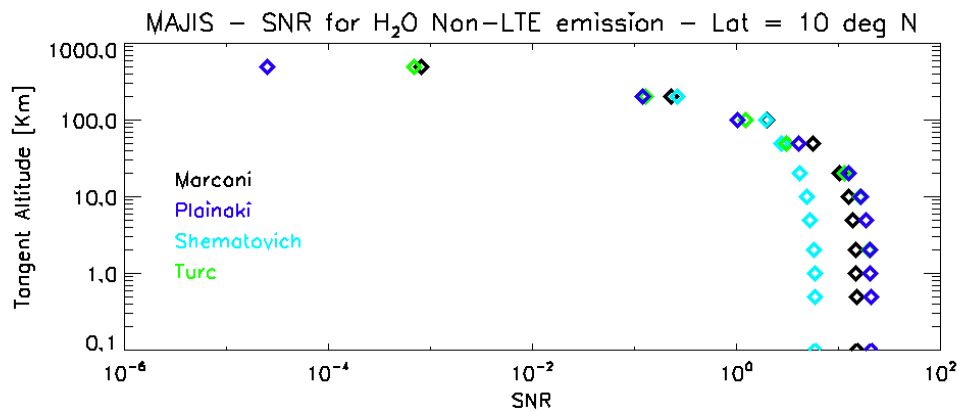
<b>Model</b>	<b>Tangent altitude (km)</b>	<b>MAJIS SNR (high vertical res.)</b>	<b>MAJIS SNR (low vertical res.)</b>
Marconi (2007)	10	12.6	178
Marconi (2007)	50	5.62	79.2
Marconi (2007)	100	1.98	27.8
Plainaki et al. (2015)	10	16.6	234
Plainaki et al. (2015)	50	4.07	57.2
Plainaki et al. (2015)	100	1.03	14.4
Shematovich (2016)	10	4.82	67.9
Shematovich (2016)	50	2.73	38.5
Shematovich (2016)	100	1.94	27.3
Turc et al. (2014)	10	16.0	225.8
Turc et al. (2014)	50	3.08	43.3
Turc et al. (2014)	100	1.22	17.1

549 Figure 6 shows the estimated SNR as a function of wavelength for high vertical resolution with  
 550 different exosphere models. Our simulations using the models by Marconi (2007), Plainaki et al.  
 551 (2015), Shematovich (2016), and Turc et al. (2014), indicate that MAJIS provides outstanding  
 552 capabilities for observing water in Ganymede's exosphere in limb observations at tangent altitudes  
 553 below 100 km from the surface and at latitudes  $\pm 10^\circ$ . The upcoming measurements with JUICE of  
 554 Ganymede's exosphere are therefore expected to represent a significant test for the currently available  
 555 exospheric models providing at the same time important feedback for developing more  
 556 comprehensive scenarios.



562 **Figure 5:** Simulated MAJIS spectrum (black line, IR channel, nominal detector temperature = 90 K)  
563 of the H<sub>2</sub>O Non-LTE emission between 2.4 and 3 microns for the Ganymede exosphere model by  
564 Plainaki et al. (2015) at lat~10°N and tangent altitudes of 1, 10, 20, 50, and 100 km. Red line indicates  
565 the predicted Noise Equivalent Spectral Radiance (NESR) of the MAJIS instrument for high vertical  
566 resolution observations.

567



568

569 **Figure 6:** Comparison of the MAJIS signal-to-noise ratios for H<sub>2</sub>O non-LTE emission for high  
570 vertical resolution observations computed for different exospheric models as a function of  
571 observation tangent altitude at latitude ~10° N. See text for details.

572

573 Several parameters related to the water deposition on the surface (e.g., the spatial distribution of the  
574 H<sub>2</sub>O abundance on Ganymede's surface, the albedo map) are expected to be linked to the impact of  
575 the external environment. Recently, studies based on VLT/SINFONI data (1.40–2.50  $\mu$ m) showed  
576 that the abundance maps of H<sub>2</sub>O-ice on Ganymede's surface are characterized by a latitudinal gradient  
577 linked to the magnetosphere ion bombardment (Ligier et al. 2019). Prior to this study, Khurana et al.  
578 (2007) had shown that there is a good correlation between the position of the OCFB and the boundary  
579 of Ganymede's polar cap, suggesting that this is evidence of the effect of charged particles impacting  
580 the moon's surface. Khurana et al. (2007) suggested also that the equatorial leading/trailing  
581 asymmetry was due to the preferential flux of ions. Sputtering can remove part of the surface upper  
582 layers allowing the underlying fresh ice to emerge and be subsequently released in the exosphere. So,

the related redistribution of water frost on the surface (due to sputtering and also water deposition from the exosphere) is expected to cause a surface brightening that is well correlated with the ion precipitation patterns and the sputtered-H<sub>2</sub>O water exosphere. Moreover, radiation can also have an impact on the structure of surface water ice: indeed, the existence of amorphous ice –mostly in the first micrometer layers is due to higher radiation processing (Hansen and McCord, 2004; 720 Famà et al. 2010). Therefore, observing with MAJIS the surface regions that are expected to be mostly bombarded by Jupiter’s magnetospheric ions should provide also an indication of the expected water deposition from the exosphere itself. Moreover, almost simultaneous observations of Ganymede’s exosphere and surface with MAJIS could allow to infer about the link between them in terms of water deposition, especially if performed at different locations.

593

#### 594 **4. Possible detectability of Ganymede’s plumes**

595

Currently, there is no empirical evidence for the presence of plumes at Ganymede. However, lessons learned from both Enceladus, where active plumes have been imaged by the ISS camera and the VIMS spectrometer on board the Cassini spacecraft (Porco et al., 2006; Hedman, 2009), and Europa (Roth et al., 2014; Sparks et al., 2016; Jia et al., 2018; Paganini et al., 2019), provide a good motivation for estimating the plume detection capability at Ganymede by the instruments on board JUICE.

602

In principle, MAJIS (as the JANUS camera) can detect plumes through the scattering of solar light by plume grains. In the range of grain size inferred at Enceladus (radii of about 2-5  $\mu\text{m}$ ), the scattering efficiency is strongly peaked in the forward direction, making the detection of plumes much more likely in high solar phase angle configurations. Therefore, optimal conditions for plume detection with MAJIS are the limb viewings at high phase angle and with a spatial resolution high enough to resolve the plume in its vertical extension. In both Enceladus and Europa cases, plume heights have

609 been estimated to be of the order of 100-200 km (e.g., Roth et al., 2014) and this scale length is  
 610 assumed as an upper limit on Ganymede.

611

612 On the basis of the currently planned trajectories of spacecraft, the above mentioned observing  
 613 constraints are expected to be achieved several times along the JUICE mission, during Ganymede  
 614 flybys as well as during the Ganymede orbital phase. The different opportunities mainly differ in the  
 615 observing range, varying from  $2 \cdot 10^5$  km to 4000 km, yielding large variations of spatial resolution.  
 616 We show here the evaluation of the detection limits on the plume density in three different  
 617 configurations of MAJIS observations, taken as study cases: (a) a distant flyby, (b) a close flyby, and  
 618 (c) a high orbit (GCO-5000). We point out that currently only case (c) is compatible with Sun  
 619 avoidance rules except when JUICE is in the shadow of Jupiter (and Ganymede is not), nevertheless,  
 620 with the scope to present better our methodology within the current paper, we speculate on all three  
 621 hypothetical cases.

622

623 In all cases, plume scattering properties are calculated using the Mie theory for spherical  
 624 homogeneous particles (Bohren and Huffman, 1983), assuming a pure water ice composition, and  
 625 grain sizes lognormally distributed with a 3  $\mu$ m effective radius and a 1.5 effective variance. The  
 626 solar radiance scattered by the plume is evaluated in a single scattering approximation as

$$627 \quad I_{pl}(\lambda) = \frac{1}{4\pi} F_{sun}(\lambda) \underline{C_{sca}}(\lambda) \underline{P}(\lambda, \alpha) N_{pl} f_f \quad (5)$$

628

629 being  $F_{sun}(\lambda)$  the solar radiance at the actual heliocentric range,  $\underline{C_{sca}}(\lambda)$  and  $\underline{P}(\lambda, \alpha)$  respectively the  
 630 single scattering cross section and single scattering phase function of the plume particles, averaged  
 631 over their size distribution,  $N_{pl}$  the plume number column density, and  $f_f$  the filling factor of the  
 632 MAJIS pixel. The latter is computed as the fraction of the MAJIS instantaneous field-of-view  
 633 intersecting a cylindrical homogeneous plume, 200 km in height and 10 km in diameter. With this

634 assumption the filling factor equals unity for observing distances less than about 65000 km. Plume  
635 particles thermal emission intensity is estimated below 1% of the solar scattered radiation levels for  
636 wavelengths shortward of 5  $\mu\text{m}$  (assuming a 120 K grain temperature), and is therefore neglected.  
637 Expected noise levels for plume observations, taking into account the source, background, and dark  
638 current noise sources assuming a detector temperature of 130 K for the MAJIS VIS-NIR channel (see  
639 Table 2), are evaluated as a function of the plume column density (in the line-of-sight direction) and  
640 exposure times. The resulting SNR appears higher in the 0.8-1.0  $\mu\text{m}$  wavelength range, and the  
641 average SNR value in that range is used to define plume detection limits.

642  
643 The results for the three study cases here considered are shown in Figure 7, for a range of MAJIS  
644 exposure times (no despiking processing included) and plume column densities, while the  
645 corresponding observing parameters are summarized in Table 4. The red, orange, and green thick  
646 lines indicate the column density detectable with a SNR level of 1, 2, or 3 respectively. For  
647 comparison, the range of plume densities estimated for the Enceladus case (Porco et al., 2006) are  
648 indicated by the blue-filled region.

649 Our analysis shows that the b) case (close flyby) is the most favorable one, since the simultaneous  
650 optimization of both resolution and phase angle enables the detection of low density plumes, 1-2  
651 orders of magnitudes thinner than Enceladus ones, even with short integration times. In the a) case  
652 (distant flyby) the increase of observing distance pertaining to high phase angles makes the plume  
653 subpixel, and detection of thin features requires integration times longer than about 10 sec. The c)  
654 case (high-altitude orbit phase) appears the worst one, since even the detection of a high-density  
655 (Enceladus-like) plume requires very long integration times. It is interesting to note that the lower  
656 detection probability in the c) case is due to the smaller phase angle achievable in the orbit phase,  
657 which are predicted to not overcome the  $140^\circ$  value. A better performance may be achieved in this  
658 phase if the plume contains a significant population of submicron grains, whose forward scattering  
659 peak is less pronounced.



660 It is worth stressing that these estimations are based on the currently available radiometric model of  
 661 the instrumental response, while more quantitative predictions require the actual instrumental  
 662 response which will be measured after the integration of the MAJIS flight-model.

663

**Table 4:** Detectability of Ganymede plumes: parameters used for detection limits  
 estimations for the three hypothetical study cases

Study case	S/c distance	Solar phase angle	Heliocentric distance	Spatial resolution	Filling factor for MAJIS pixel
a) distant flyby case (Dec. 2030)	189000 km	174°	5.33 AU	28 km/pixel	0.35
b) close flyby case (Sep. 2030)	4500 km	175°	5.37 AU	0.7 km/pixel	1.0
c) high orbit case (Nov. 2032)	7700 km	135°	5.10 AU	1.2 km/pixel	1.0

664

665

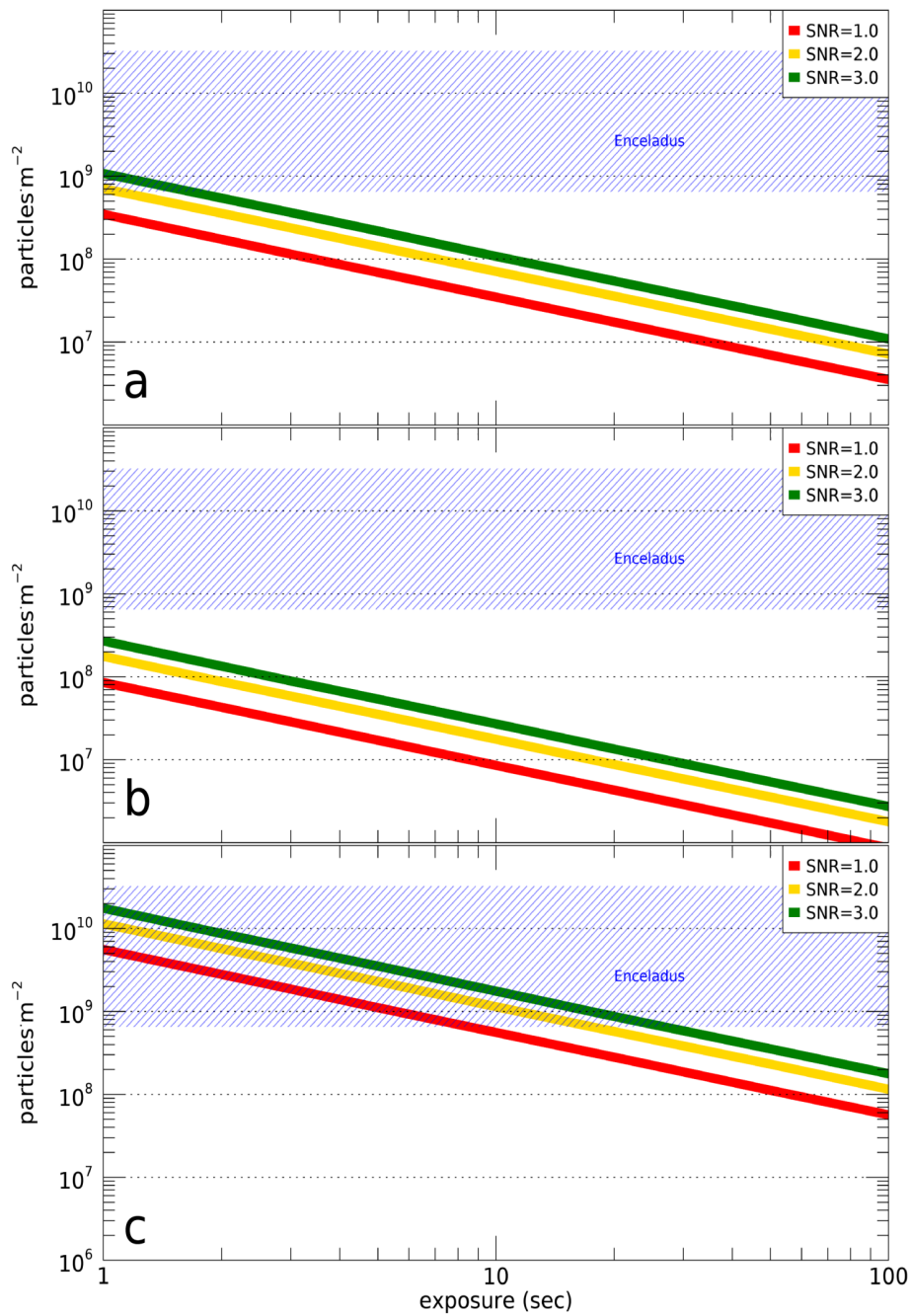


**Figure 7:** Detectability of a water ice plume in the three different study cases described in text and Table 4 and representing conditions encountered during different JUICE mission phases: distant flyby (panel a), close flyby (panel b), high orbit (panel c). Red, orange, and green lines indicate the plume column density detectable with SNR values of 1, 2, or 3, respectively (as average value in the 0.8-1.0  $\mu\text{m}$  range). The blue-filled regions show the range of densities of the Enceladus plume. The despiking process has not been taken into account.

## 668 5. Discussion and Conclusions

669

670 Lunar exospheres are important sources of neutral gas in the outer Solar System often associated with  
671 the formation of torus-shaped clouds (e.g., Mauk et al., 2003; Shematovich, 2016). They play an  
672 important role in the balance between the neutral gas and magnetospheric plasma in the giant  
673 planetary systems. The determination of the properties of the exospheric environment provides the  
674 necessary information to better understand the weathering processes induced on ice by the radiation  
675 environment.

676

677 Surface sputtering and water sublimation play a key role in the generation and dynamical evolution  
678 of Ganymede's exosphere. In general, numerical models simulating the generation of Ganymede's  
679 surface-bounded H<sub>2</sub>O exosphere agree that thermal ion populations provide a minor contribution to  
680 the total sputtering rate with respect to heavy energetic ions (e.g., Sulfur ions and Oxygen ions).  
681 Water sublimation is expected to be the dominant surface release process only locally, although some  
682 uncertainty in the considered rates exists due to the lack of quantitative information on the surface  
683 impurities concentration and actual temperature. For comparison, on Saturn's moon Tethys the  
684 intense bombardment of high-energy magnetospheric electrons collimated on the leading hemisphere  
685 of the moon is the driving mechanism causing the formation of the equatorial lens and nearby  
686 "Pacman" feature (Howett, 2012). As a consequence of the electrons bombardment, the ice grains  
687 displaced on the regolith are sinthered together (Filacchione et al., 2018), forming larger grains and  
688 causing local thermophysical anomalies: the lens appears in fact colder (Howett et al., 2012;  
689 Filacchione et al., 2016) and darker (Schenk et al., 2011; Filacchione et al., 2018) with respect to  
690 nearby regions not altered by the electron flux. Exospheric models for Ganymede (e.g., Marconi  
691 2007; Turc et al., 2014; Plainaki et al., 2015; Shematovich 2016; Leblanc et al., 2017) generally  
692 almost agree in terms of water release rate from the surface and maximum H<sub>2</sub>O vapor density,  
693 however, the different assumptions in each model result in different density profiles. Future

34

694 experimental work in estimating ice sputtering and radiolysis yields and even more accurate  
695 estimations of the exosphere sources (e.g., through the consideration of the entire energy range of the  
696 impinging ions) and loss rates (e.g., through the definition of the precise morphology of the plasma  
697 around Ganymede) will certainly help to better estimate the vapor H<sub>2</sub>O density distribution.

698

699 In this work, we provided a first evaluation of the potential of observing Ganymede's H<sub>2</sub>O exosphere  
700 with JUICE/MAJIS. Our main motivation for this exercise was the possibility to obtain IR radiation  
701 measurements that will constrain the efficiency and morphology of the surface particle release as well  
702 as the energy exchange between the Jovian system and the moon. Two representative observation  
703 cases have been considered for observations from GCO-5000, one at high vertical resolution  
704 (projected IFOV of ~1.1 km) and one at low vertical resolution (projected IFOV of ~10 km). The  
705 results of our estimations provide evidence that given the specifications of MAJIS, the instrument has  
706 the necessary sensitivity to observe the moon's water vapor environment with a SNR higher than 1  
707 during limb observations with tangent altitude below 100 km from the surface and at latitudes  $\pm 10^\circ$ ,  
708 even when considering the model leading to the lowest column densities of water vapor. If current  
709 exospheric models are correct, and in absence of plumes, we confirm that the H<sub>2</sub>O exosphere to be  
710 detected with MAJIS will be the one generated through water ice sublimation, since the SNR  
711 corresponding to the sputtered water component is expected to be extremely low. Even if this were  
712 the case, the possible investigation of Ganymede's exosphere with MAJIS is still important since it  
713 can provide useful information for speculating on the surface weathering processes. We note that the  
714 deposition of neutral species from the exosphere onto the moon's surface can spectrally mask the  
715 weathering products or directly start new chemical patterns. Therefore, to understand the processes  
716 of weathering we need first to characterize the moon's exosphere, even if only locally. Based on the  
717 above, the most favorable observation condition during JUICE is the one focused on the region  
718 around the subsolar point. For limb observations, MAJIS would require setting its slit tangent to the  
719 limb, a configuration that avoids saturation from the satellite if the limb is sunlit, providing at the

720 same time optimum vertical resolution with spatial binning. Potential joint-observations between  
721 MAJIS and UVS are likely to increase the scientific return from the observation of Ganymede's  
722 exosphere. We note here that the estimations in the current paper are likely to be revised in the next  
723 years also due to theoretical model updates hence our results provide a first indicative range for the  
724 expected exospheric measurements. The upcoming measurements with JUICE will provide proof of  
725 the most realistic scenario among the ones currently proposed for the exosphere of Ganymede.

726

727 Considering the potential detection of plumes at Ganymede (if any), we showed that particular  
728 combination of resolution and phase angle shall enable to optimize the MAJIS observation and  
729 resulting SNR of low density plumes. The simulation indicates that MAJIS can detect plumes of  
730 density 1-2 orders of magnitudes thinner than the Enceladus ones by optimizing the integration times  
731 and selecting the VISNIR channel. Further detailed work in this direction is strongly required to take  
732 into consideration the expected properties of a potential plume at Ganymede (considering also the  
733 role of the moon's orbit phase around Jupiter), as well as the real performances of the instrument after  
734 characterization, the validation of the despiking algorithm once in flight, and (during Ganymede  
735 encounters), the compatibility between the necessary (for the observations) phase angles and the Sun  
736 avoidance rules requested by MAJIS. Potential planning for a series of observations at different  
737 latitudes together with JANUS, as done in the past for Enceladus by ISS and VIMS onboard Cassini  
738 (Hedman et al., 2009) will help us to better understand the properties of plumes (if any) and, possibly,  
739 their variability in time. Future work in this direction is intended.

740

741 There are some drawbacks related to the estimations presented in this paper. First, the current study  
742 considers as inputs the outputs of numerical simulations hence the differences among the obtained  
743 calculations cannot be neither rigorously nor easily attributed to specific parameters within each  
744 model. Different theoretical models of the H<sub>2</sub>O exosphere, and different configurations between  
745 Ganymede, Jupiter and the Sun may result in different exosphere morphologies (see, for example,

746 Leblanc et al., 2017) hence this study provides only a preliminary and rough estimation of the  
747 expected measurement by MAJIS. Indeed, Ganymede's magnetosphere changes continuously due to  
748 the moon's motion above and below the Jupiter plasma sheet but also due to the variation of the  
749 plasma sheet properties itself. Recently, Vogt et al. (2017) found that Jupiter's current sheet current  
750 density parameter varies by  $\sim 15\text{--}20\%$  with respect to its average value. The exosphere is expected to  
751 be influenced by such changes in terms of both generation and loss process efficiency. The study of  
752 the variation of the exosphere due to variations of the space environment external to Ganymede  
753 (planetary space weather) is an important requisite for future estimations of its detectability and for  
754 optimizing the observational conditions. Second, all the exospheric models considered in this study  
755 assume that the  $\text{H}_2\text{O}$  sublimation rate above the subsolar point is relatively high. Unfortunately, there  
756 are currently no published observational evidences that prove (or deny) this fact. At a larger  
757 perspective, future exploration of the Outer Solar System requires knowledge on the planetary space  
758 weather conditions near and within the system under investigation (for a more detailed discussion in  
759 this context see Plainaki et al. (2016) and references therein). Last, our estimations show that the  
760 dominant component to be observed with MAJIS is likely sublimated  $\text{H}_2\text{O}$ , for which all models  
761 estimate the same maximum concentration. Although the sputtered  $\text{H}_2\text{O}$  exosphere, as estimated  
762 nowadays by models, is likely under the detectability limits of MAJIS, the remote possibility of its  
763 observation should not be ruled out. This is because ongoing laboratory work on the efficiency of  
764  $\text{H}_2\text{O}$  release from ice as well as recent estimations of updated release yields (see, for instance, Teolis  
765 et al. 2017) and of the role of the radiation environment (see, for instance, Poppe et al. 2018) and  
766 secondary sputtering (Carnielli et al., 2019) may result in an increase of the  $\text{H}_2\text{O}$  density. In such a  
767 case, the current estimations provide only a lower limit for future detection.

768

769 To accurately estimate the SNR expected for MAJIS during limb observations of Ganymede's  $\text{H}_2\text{O}$   
770 exosphere, further detailed work is required, taking also into consideration further opportunities to  
771 observe the exosphere of Ganymede. The current study, therefore, will be expanded and the results

will be integrated considering different observational opportunities during the JUICE mission. In particular, we plan to integrate in our radiance simulator the actual MAJIS observational geometries (incidence and emission angles, tangent altitudes, spacecraft distances, etc.) based on the Consolidated Report on Mission Analysis (CReMA; Boutonnet and Schoenmaekers, 2012) trajectories and the instrument pointing abilities. Such an approach will provide feedback for driving the MAJIS observational planning in order to optimize the Ganymede's exosphere detection accordingly with the MAJIS spectral sensitivity.

## References

Bagenal, F., Wilson, R. J., Siler, S., Paterson, W. R. et al., 2016. Survey of Galileo plasma observations in Jupiter's plasma sheet. *Journal of Geophysical Research: Planets*, 121, 871–894. [DOI: 10.1002/2016JE005009](https://doi.org/10.1002/2016JE005009)

Bahr, D. A., Famá, M., Vidal, R. A., & Baragiola, R. A., 2001. Radiolysis of water ice in the outer solar system: Sputtering and trapping of radiation products. *Journal of Geophysical Research*, 106(E12), 33,285–33,290, DOI: 10.1029/2000JE001324

Barth C.A., Hord, C.W., Stewart, A.I.F., et al. (1996). Galileo ultraviolet spectrometer observations of atomic hydrogen in the atmosphere of Ganymede. *Geophys. Res. Lett.*, 24, 2147-2150.

Bockelée-Morvan, D., 1987. A model for the excitation of water in comets. *Astronomy and Astrophysics*, 181, 1, 169-181, 1987A&A., 181..169B

Bockelée-Morvan, D., Crovisier, J., Mumma, M. J., and Weaver, H. A., 2004. The composition of cometary volatiles, in: M. C. Festou, H. U. Keller, & H. Weaver (Eds), *Comets II*, 391

Bockelée-Morvan, D., Crovisier, J., Erard, S., Capaccioni, F. et al., 2016. Evolution of CO<sub>2</sub>, CH<sub>4</sub>, and OCS abundances relative to H<sub>2</sub>O in the coma of comet 67P around perihelion from

797 *Rosetta/VIRTIS-H observations, Monthly Notices of the Royal Astronomical Society*, 462, Suppl\_1,  
798 S170–S183, [DOI: 10.1093/mnras/stw2428](https://doi.org/10.1093/mnras/stw2428)

799 Bohren C. F., Huffman D. R., 1983. Absorption and Scattering of Light by Small Particles.  
800 Wiley, New York

801 Boutonnet, A., Schoenmaekers, J.: JUICE: Consolidated Report on Mission Analysis (CReMA  
802 ), ESA, 2012

803 Broadfoot A. L., Belton M. J., Takacs P. Z., Sandel B. R. et al., 1979. Extreme ultraviolet  
804 observations from Voyager 1 encounter with Jupiter. *Science*, 204:979–982,  
805 DOI:10.1126/science.204.4396.979

806 Coustenis, A., Atreya, S., Castillo, J., Coll, P., 2010. Surfaces and atmospheres of the outer  
807 planets, their satellites and ring systems: Part VI , *Planetary and Space Science*, 58, 13, 1665-1666,  
808 DOI: 10.1016/j.pss.2010.09.00

809 Crovisier, J., 1987. Rotational and vibrational synthetic spectra of linear parent molecules in  
810 comets, *Astronomy and Astrophysics Supplement Series* (ISSN 0365-0138), 68, 2, 223-258,  
811 Bibcode: 1987A&AS...68..223C

812 Famà, M., Shi, J., Baragiola, R.A., 2008. Sputtering of ice by low-energy ions. *Surf. Sci.*  
813 602, 156–161, DOI: 10.1016/j.susc.2007.10.002

814 Fatemi, S., Poppe, A. R., Khurana, K. K., Holmström, M. et al., 2016. On the formation of  
815 Ganymede’s surface brightness asymmetries: Kinetic simulations of Ganymede’s magnetosphere.  
816 *Geophysical Research Letters*, 43, 4745–4754, DOI: 10.1002/2016GL068363

817 Feldman, P.D., McGrath, M.A., Strobel, D.F., Moos, H.W., Retherford, K.D., Wolven, B.C.,  
818 2000. HST/STIS ultraviolet imaging of polar Aurora on Ganymede, *Astrophys. J.*, 535, 1085–1090,  
819 DOI: 10.1086/308889.

820 Filacchione, G., D’Aversa, E., Capaccioni, F., Clark, R.N. et al. (2016). Saturn’s icy satellites  
821 investigated by Cassini-VIMS. IV. Daytime temperature maps. *Icarus*, 271, 292–313, DOI:  
822 10.1016/j.icarus.2016.02.019



823 Filacchione, G., Ciarniello, M., D'Aversa, E., Capaccioni, F. et al., 2018. Photometric modeling  
824 and VIS-IR Albedo maps of Tethys from Cassini-VIMS. *Geophysical Research Letters*, 45, 6400–  
825 6407, DOI: 10.1029/2018GL078602.

826 Gordon, I.E., Rothman, L.S., Hill, C., Kochanov, R.V. et al., 2017. The HITRAN2016 molecular  
827 spectroscopic database, *Journal of Quantitative Spectroscopy and Radiative Transfer*, 203, 3-69, DOI:  
828 10.1016/j.jqsrt.2017.06.038

829 Grasset, O., Dougherty, M.K., Coustenis, A., Bunce, E.J., et al., 2013. Jupiter Icy moons  
830 Explorer (JUICE): an ESA mission to orbit Ganymede and to characterize the Jupiter system. *Planet.*  
831 *Space Sci.*, 78,1–21, DOI: 10.1016/j.pss.2012.12.002

832 Guerri, I., Fabbri, A., Tommasi, L., Taiti, A. et al., 2018. The optical design of the MAJIS  
833 instrument on board of the JUICE mission, *Proc. SPIE 10690, Optical Design and Engineering VII*,  
834 106901L (5 June 2018), doi:10.1117/12.2312013

835 Gurnett, D.A., Kurth, W.S., Roux, A., Bolton, S.J., Kennel, C.F., 1996. Evidence for a  
836 magnetosphere at Ganymede from plasma-wave observations by the Galileo spacecraft. *Nature*, 384,  
837 535–537, DOI: 10.1038/384535a0.

838 Hall, D.T., Feldman, P.D., McGrath, M.A., Strobel, D.F., 1998. The far-ultraviolet oxygen  
839 airglow of Europa and Ganymede. *Astrophys. J.*, 499, 475–481, DOI: 10.1086/305604

840 Hartogh et al., 2013  
841 [http://herschel.esac.esa.int/TheUniverseExploredByHerschel/presentations/13a-](http://herschel.esac.esa.int/TheUniverseExploredByHerschel/presentations/13a-1720_HartoghP.pdf)  
842 [1720\\_HartoghP.pdf](http://herschel.esac.esa.int/TheUniverseExploredByHerschel/presentations/13a-1720_HartoghP.pdf)

843 Hedman, M.M., Nicholson, P.D., Showalter, M.R., Brown, R.H., Buratti, B.J., Clark, R.N. 2009.  
844 Spectral observations of the Enceladus plume with Cassini-VIMS. *ApJ*, 693, 1749-1762, DOI:  
845 10.1088/0004-637X/693/2/1749

846 Howett, C. J. A., Spencer, J. R., Hurford, T., Verbiscer, A., & Segura, M. (2012). PacMan  
847 returns: An electron-generated thermal anomaly on Tethys. *Icarus*, 221, 1084–1088, DOI:  
848 10.1016/j.icarus.2012.10.013

849 Jia, X., Walker, R.J., Kivelson, M.G., Khurana, K.K., Linker, J.A., 2008. Three-dimensional  
850 MHD simulations of Ganymede's magnetosphere. *J. Geophys. Res. Space Physics*, 113, A06212,  
851 DOI: 10.1029/2007JA012748.

852 Jia, X., Walker, R.J., Kivelson, M.G., Khurana, K.K., Linker, J.A., 2009. Properties of  
853 Ganymede's magnetosphere inferred from improved three-dimensional MHD simulations. *J.*  
854 *Geophys. Res. Space Physics*, 114, A09209, DOI: 10.1029/2009JA014375.

855 Jia, X., Kivelson, M.G., Khurana, K.K., Kurth, W.S. 2018. Evidence of a plume on Europa from  
856 Galileo magnetic and plasma wave signatures. *Nature Astronomy*, 2, 459–464, DOI:  
857 10.1038/s41550-018-0450-z

858 Johnson, R. E., 1990. Interactions with surfaces. *Energetic charged-particle interactions with*  
859 *atmospheres and surfaces* (pp. 75–135). Berlin: Springer-Verlag

860 Khurana, K. K., Pappalardo, R. T., Murphy, N., & Denk, T., 2007. The origin of Ganymede's  
861 polar caps. *Icarus*, 191, 193–202, DOI: 10.1016/j.icarus.2007.04.022

862 Kivelson, M. G., Bagenal, F., Kurth, W. S., Neubauer, F. M., Paranicas, C., & Saur, J. (2004).  
863 *Magnetospheric interactions with satellites, Jupiter: The planet, satellites, and magnetosphere* (pp.  
864 513–536). Cambridge, UK: Cambridge University Press.

865 Kivelson, M. G., Khurana, K. K., Russell, C. T., Walker, R. J. et al., 1996. Discovery of  
866 Ganymede's magnetic field by the Galileo spacecraft. *Nature* 384, 537–541, DOI: 10.1038/384537a0

867 Kivelson, M.G., Khurana, K.K., Coroniti, F.V., Joy, S. et al., 1997. Magnetic field and  
868 magnetosphere of Ganymede. *Geophys. Res. Lett.* 24, 2155, DOI: 10.1029/97GL02201

869 Langevin, Y., Piccioni, G., Filacchione, G., Poulet, F. & Dumesnil, C., 2018. MAJIS, the VIS-  
870 IR imaging spectrometer of JUICE, IPM 2018, E1.

871 Langevin, Y., Piccioni, G. and the MAJIS Team, 2017. The MAJIS visible/NIR imaging  
872 spectrometer on board the ESA JUICE mission : updated design, implications for performances and  
873 science goals, EPSC2017-931.

874 Leblanc, F., Oza, A.V., Leclercq, L., Schmidt, C. et al. 2017. On the orbital variability of  
875 Ganymede's atmosphere, *Icarus*, 293, 185-198, DOI: 10.1016/j.icarus.2017.04.025

876 Ligier, N., Paranicas, C., Carter, J., et al. 2019. Surface composition and properties of Ganymede:  
877 Updates from ground-based observations with the near-infrared imaging spectrometer  
878 SINFONI/VLT/ESO, *Icarus*, 333, 496, DOI:10.1016/j.icarus.2019.06.013

879 Lucchetti, A., Plainaki, C., Cremonese, G., Milillo, A. et al. 2016. Loss rates of Europa's  
880 exosphere, *PSS*, 130, 14–23, doi:10.1016/j.pss.2016.01.009

881 Marconi, M.L., 2007. A kinetic model of Ganymede's atmosphere. *Icarus*, 190, 155–174, DOI:  
882 10.1016/j.icarus.2007.02.016

883 Moore, M. H., Hudson, R. L., Carlson, R.W., 2007. The radiolysis of SO<sub>2</sub> and H<sub>2</sub>S in water ice:  
884 Implications for the icy Jovian satellites. *Icarus*, 189, 409–423, DOI: 10.1016/j.icarus.2007.01.018

885 Orton, G.S., Spencer, J.R., Travis, L.D., Martin, T.Z. et al. 1996. Galileo photopolarimeter–  
886 radiometer observations of Jupiter and the Galilean satellites. *Science* 274, 389–392.

887 Paganini, L., Villanueva, G.L., Roth, L., Mandell, A.M., Hurford, T.A. et al. 2019. A  
888 measurement of water vapour amid a largely quiescent environment on Europa, *Nature Astronomy*,  
889 DOI: 10.1038/s41550-019-0933-6

890 Paranicas, C., Paterson, W.R., Cheng, A.F., Mauk, B.H. et al., 1999. Energetic particle  
891 observations near Ganymede., *J. Geophys. Res.* 104, 17459–17470, DOI: 10.1029/1999JA900199.

892 Piccioni, G., Langevin, Y., Filacchione, G., Poulet, F. et al., 2014. MAJIS, the Moons And Jupiter  
893 Imaging Spectrometer, designed for the future ESA/JUICE mission, EGU General Assembly  
894 Conference Abstracts, 16, 10925.

895 Piccioni, G., Tommasi, L., Langevin, Y., Filacchione, G., et al., 2019. Scientific goals and  
896 technical challenges of the MAJIS imaging spectrometer for the JUICE mission. *Proceedings of the*  
897 *2019 IEEE 5th International Workshop on Metrology for AeroSpace*, Turin (Italy), 19-21 June 2019.  
898 DOI: 10.1109/MetroAeroSpace.2019.8869566.

899 Plainaki, C., Milillo, A., Mura, A., Orsini, S. et al., 2010. Neutral particle release from Europa's  
900 surface. *Icarus* 210, 385–395, DOI: 10.1016/j.icarus.2010.06.041

901 Plainaki, C., A. Milillo, A. Mura, S. Orsini, S. et al., 2012. The role of sputtering and radiolysis  
902 in the generation of Europa exosphere. *Icarus*, 218, 2, 956–966, DOI: 10.1016/j.icarus.2012.01.023

903 Plainaki, C., Milillo, A., Mura, A., Saur, J. et al., 2013. Exospheric O<sub>2</sub> densities at Europa  
904 during different orbital phases, *Planet. Space Sci.*, 88, 42, DOI: 10.1016/j.pss.2013.08.011

905 Plainaki, C., Milillo, A., Massetti, S., Mura, A. et al., 2015. The H<sub>2</sub>O and O<sub>2</sub> exospheres of  
906 Ganymede: the result of a complex interaction between the Jovian magnetospheric ions and the icy  
907 moon. *Icarus*, 245, 306–319, DOI: 10.1016/j.icarus.2014.09.018

908 Plainaki, C., Lilensten, J., Radioti, A., Andriopoulou, M. et al., 2016. Planetary space weather:  
909 scientific aspects and future perspectives, *J. Space Weather Space Clim.*, 6, A31, 2016, DOI:  
910 10.1051/swsc/2016024

911 Plainaki, C., Cassidy, T.A., Shematovich, V.I., Milillo, A. et al., 2018. Towards a Global Unified  
912 Model of Europa's Tenuous Atmosphere, *Space Sci Rev*, 214: 40, DOI: 10.1007/s11214-018-0469-6

913 Poppe, A. R., Fatemi, S., Khurana, K.K., 2018. Thermal and energetic ion dynamics in  
914 Ganymede's magnetosphere. *Journal of Geophysical Research: Space Physics*, 123, 4614–4637,  
915 DOI: 10.1029/2018JA025312

916 Porco, C.C., Helfenstein, P., Thomas, P.C., Ingersoll, A.P. et al., 2006. Cassini observes the  
917 active south pole of Enceladus, *Science*, 311, 1393–1401, DOI: 10.1126/science.1123013

918 Roth, L., Saur, J., Retherford, K.D., Strobel, D.F. et al., 2014. Transient Water Vapor at Europa's  
919 South Pole, *Science*, 343, 171–174, doi: 10.1126/science.1247051

920 Schenk, P., Hamilton, D. P., Johnson, R. E., McKinnon, W. B. et al., 2011. Plasma, plumes and  
921 rings: Saturn system dynamics as recorded in global color patterns on its midsize icy satellites. *Icarus*,  
922 211, 740–757, DOI: 10.1016/j.icarus.2010.08.016

923 Shematovich, V.I., 2016. Neutral atmosphere near the icy surface of Jupiter's moon Ganymede,  
924 *Solar System Research*, 50, 4, 262–280, DOI: 10.1134/S0038094616040067

925 Smith, B. A., Soderblom, L. A., Beebe, R., Boyce, J. et al., 1979. The Galilean satellites and  
 926 Jupiter: Voyager 2 Imaging Science results, *Science*, 206(4421), 927–950  
 927 Sparks, W. B., Hand, K. P., McGrath, M.A., Bergeron, E. et al., 2016. Probing for evidence of  
 928 plumes on Europa with HST/STIS. *Astrophys.Journ.*, 829,121, DOI: 10.3847/0004-637X/829/2/121  
 929 Sparks, W. B. et al. 2017. Active Cryovolcanism on Europa? *ApJL* 839 L18., DOI:  
 930 10.3847/2041-8213/aa67f8  
 931 Teolis, B. D., Loeffler, M. J., Raut, U., Famá, M. et al., 2006. Ozone synthesis on the icy  
 932 satellites. *The Astrophysical Journal*, 644, L141–L144.  
 933 Teolis, B. D., Plainaki, C., Cassidy, T. A., Raut, U., 2017. Water ice radiolytic O<sub>2</sub>, H<sub>2</sub>, and H<sub>2</sub>O<sub>2</sub>  
 934 yields for any projectile species, energy, or temperature: A model for icy astrophysical bodies. *Journal*  
 935 *of Geophysical Research: Planets*, 122, 1996–2012, DOI: [10.1002/2017JE005285](https://doi.org/10.1002/2017JE005285)  
 936 Turc, L., Leclercq, L., Leblanc, F., Modolo, R. et al., 2014. Modelling Ganymede’s neutral  
 937 environment: A 3D test-particle simulation, *Icarus*, 229, 157–169, DOI: 10.1016/j.icarus.2013.11.005  
 938 Villanueva G. L., Mumma M. J., Bonev B. P., Novak R.E. et al., 2012. Water in planetary and  
 939 cometary atmospheres: H<sub>2</sub>O/HDO transmittance and fluorescence models, *J. Quant. Spectrosc.*  
 940 *Radiat. Transf.*, 113, 202, DOI: 10.1016/j.jqsrt.2011.11.001  
 941 Vogt, M.F., Bunce, E.J., Nichols, J.D., Clarke, J.T. et al., 2017. Long-term variability of  
 942 Jupiter’s magnetodisk and implications for the aurora, *Journal of Geophysical Research: Space*  
 943 *Physics*, 122, 12,090–12,110, DOI: 10.1002/2017JA024066  
 944 Williams, D.J., Mauk, B.H., McEntire, R.W., Roelof, E.C. et al., 1997. Energetic particle  
 945 signatures at Ganymede: Implications for Ganymede’s magnetic field. *Geophysical Research Letters*,  
 946 24(17), 2163–2166  
 947 Williams, D.J., 2001. Ganymede’s ionic radiation belts. *Geophysical Research Letters*, 28(19),  
 948 3793–3796  
 949 Williams, D. J., McEntire, R. W., Jaskulek, S., & Wilken, B. (1992). The Galileo energetic  
 950 particles detector. *Space Science Reviews*, 60, 385–412.

## APPENDIX

**Figure A1:** Simulated MAJIS spectrum (black line) of the H<sub>2</sub>O Non-LTE emission between 2.4 and 3  $\mu$ m for Ganymede's exosphere model by Marconi et al. (2007) at lat~10°N and tangent altitudes of 1, 10, 20, 50, 100 km above the surface, from top to bottom panel respectively. Red line indicates the predicted Noise Equivalent Spectral Radiance (NESR) of the MAJIS instrument for high vertical resolution observations.

**Figure A2:** Simulated MAJIS spectrum (black line) of the H<sub>2</sub>O Non-LTE emission between 2.4 and 3  $\mu$ m for Ganymede's exosphere model by Shematovich et al. (2016) at lat~10°N and tangent altitudes of 1, 10, 20, 50, 100 km above the surface, from top to bottom panel respectively. Red line indicates the predicted Noise Equivalent Spectral Radiance (NESR) of the MAJIS instrument for high vertical resolution observations.

**Figure A3:** Simulated MAJIS spectrum (black line) of the H<sub>2</sub>O Non-LTE emission between 2.4 and 3  $\mu$ m for Ganymede's exosphere model by Turc et al. (2014) at lat~10°N and tangent altitudes of 1, 10, 20, 50, 100 km above the surface, from top to bottom panel respectively. Red line indicates the predicted Noise Equivalent Spectral Radiance (NESR) of the MAJIS instrument for high vertical resolution observations.

Figure A1

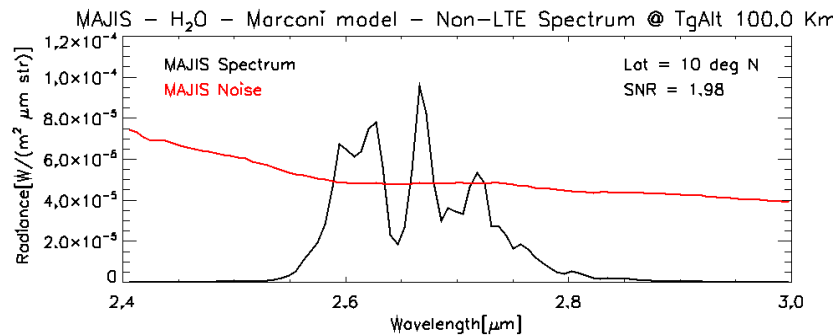
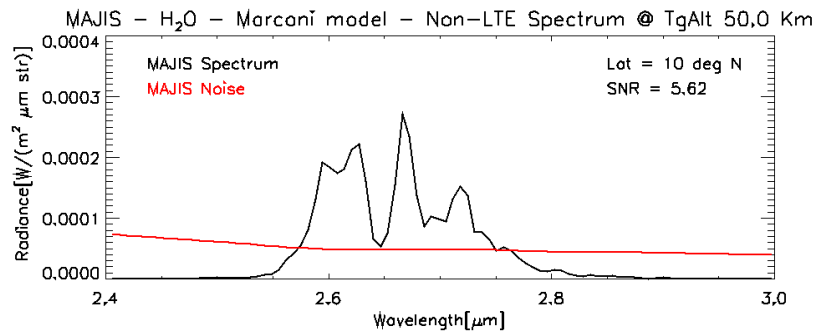
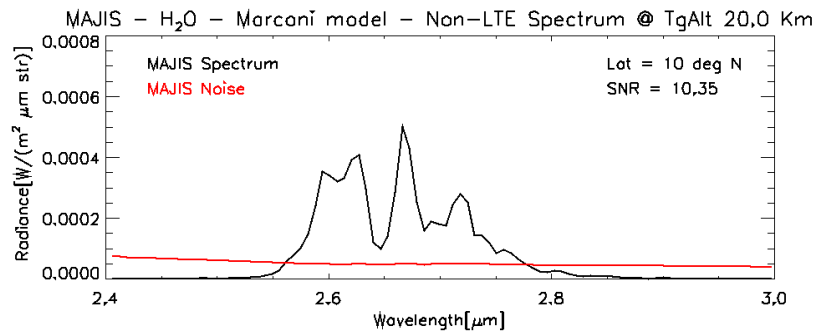
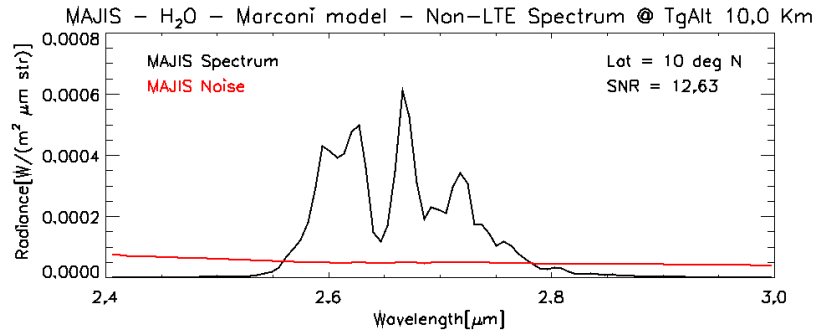
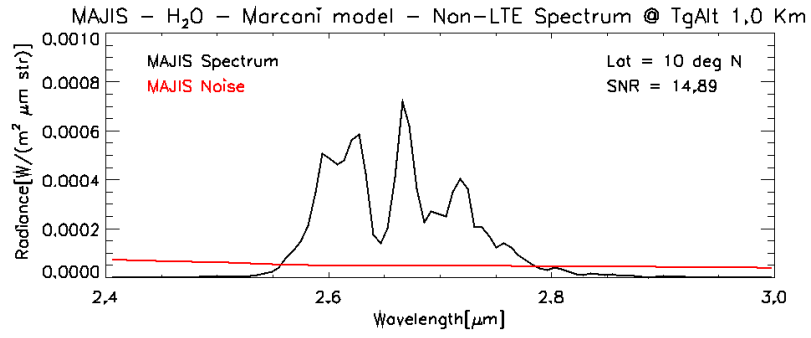


Figure A2

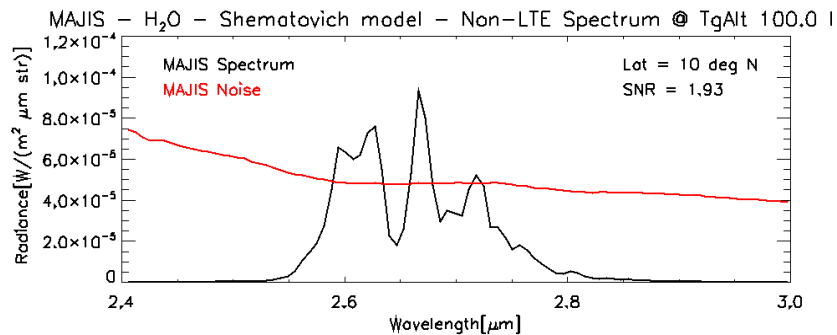
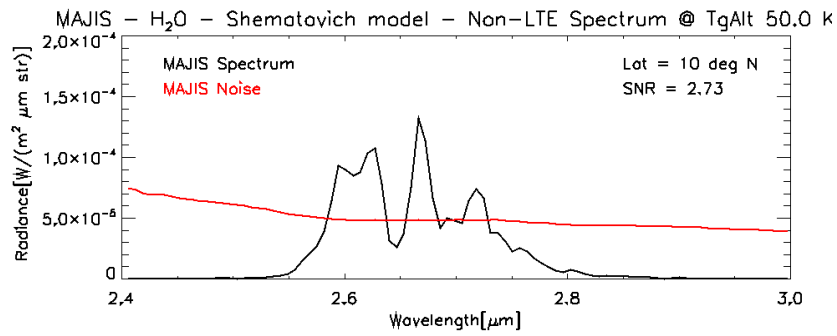
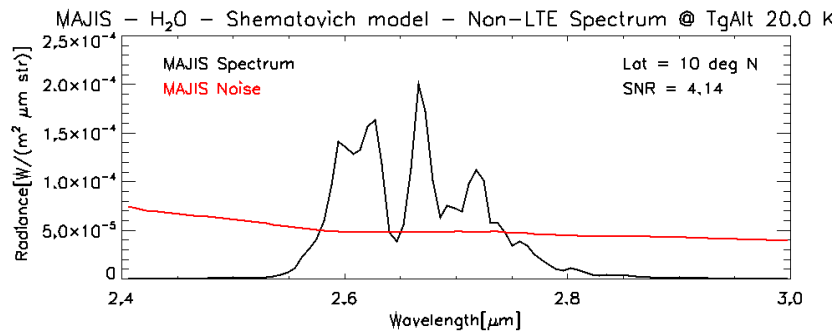
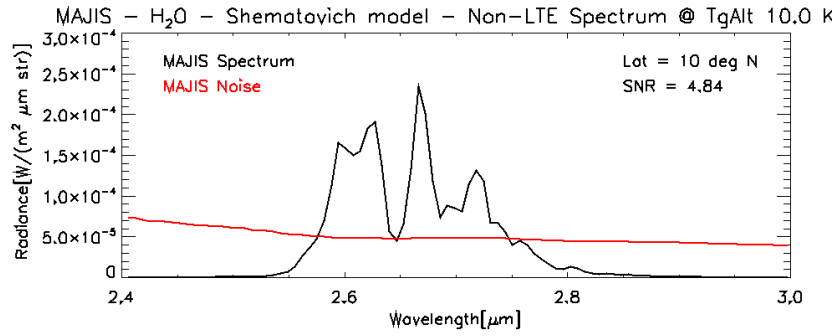
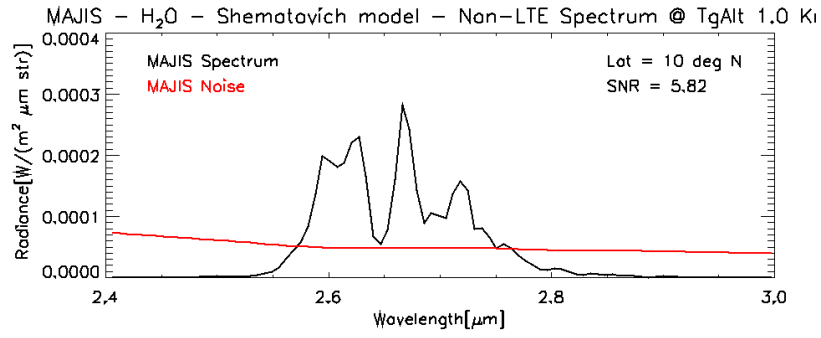




Figure A3

